Petroleum Science 22 (2025) 1062–1079

Contents lists available at ScienceDirect

Petroleum Science

journal homepage: www.keaipublishing.com/en/journals/petroleum-science

Original Paper

Dynamic reservoir monitoring using similarity analysis of passive source time-lapse seismic images: Application to waterflooding front monitoring in Shengli Oilfield, China

Ying-He Wu [a, b], Shu-Lin Pan [a], Hai-Qiang Lan [c, *], Jing-Yi Chen [d], José Badal [e], Yao-Jie Chen [a], Zi-Lin Zhang [f], Zi-Yu Qin [g]

[a] School of Earth Science and Technology, Southwest Petroleum University, Chengdu, 610500, Sichuan, China
[b] Department of Physics, Faculty of Science, University of Alberta, Edmonton, T6G 2E1, Canada
[c] State Key Laboratory of Lithospheric Evolution, Institute of Geology and Geophysics, Chinese Academy of Sciences, Beijing, 100029, China
[d] Seismic Anisotropy Group, Department of Geosciences, The University of Tulsa, Tulsa, OK 74104, USA
[e] University of Zaragoza, Sciences B, Pedro Cerbuna 12, Zaragoza, 50009, Spain
[f] Research Institute of Petroleum Engineering Technology, Sinopec Shengli Oilfield Company, Dongying, 257000, Shandong, China
[g] School of Software Engineering, Chengdu Technological University, Chengdu, 610031, Sichuan, China

ARTICLE INFO

Article history:
Received 26 April 2024
Received in revised form
28 July 2024
Accepted 9 December 2024
Available online 10 December 2024

Edited by Meng-Jiao Zhou and Min Li

Keywords:
Passive source time-lapse seismic imaging
Seismic interferometry
Dynamic reservoir monitoring
Similarity analysis
Waterflooding front monitoring
Shengli Oilfield

ABSTRACT

In common practice in the oil fields, the injection of water and gas into reservoirs is a crucial technique to increase production. The control of the waterflooding front in oil/gas exploitation is a matter of great concern to reservoir engineers. Monitoring the waterflooding front in oil/gas wells plays a very important role in adjusting the well network and later in production, taking advantage of the remaining oil potential and ultimately achieving great success in improving the recovery rate. For a long time, microseismic monitoring, numerical simulation, four-dimensional seismic and other methods have been widely used in waterflooding front monitoring. However, reconciling their reliability and cost poses a significant challenge. In order to achieve real-time, reliable and cost-effective monitoring, we propose an innovative method for waterflooding front monitoring through the similarity analysis of passive source time-lapse seismic images. Typically, passive source seismic data collected from oil fields have extremely low signal-to-noise ratio (SNR), which poses a serious problem for obtaining structural images. The proposed method aims to visualize and analyze underground changes by highlighting time-lapse images and provide a strategy for underground monitoring using long-term passive source data under low SNR conditions. First, we verify the feasibility of the proposed method by designing a theoretical model. Then, we conduct an analysis of the correlation coefficient (similarity) on the passive source time-lapse seismic imaging results to enhance the image differences and identify the simulated waterflooding fronts. Finally, the proposed method is applied to the actual waterflooding front monitoring tasks in Shengli Oilfield, China. The research findings indicate that the monitoring results are consistent with the actual development conditions, which in turn demonstrates that the proposed method has great potential for practical application and is very suitable for monitoring common development tasks in oil fields.

1. Introduction

Monitoring dynamic changes of underground reservoirs and fluid migration processes has always been an important part of the oilfield development process. Real-time dynamic reservoir monitoring can help us continuously understand oil and gas formations and injection production profile, and provide scientific guidance for oilfield development technology optimization and secondary encryption implementation (Hoover et al., 1999; De Freitas, 2011; Xu et al., 2012; Zeng et al., 2018; Wang et al., 2021). Overall, it is an important technique to improve the final recovery rate and promote the economic and rational development of oil and gas

* Corresponding author.
E-mail address: lanhq@mail.iggcas.ac.cn (H.-Q. Lan).

https://doi.org/10.1016/j.petsci.2024.12.008

resources. The development of water injection is the main exploitation technology suitable for low permeability oil fields. During the waterflooding process, the direction of water injection and the location of the flood front are important for reservoir engineers to design and adjust development plans (Jackson and Muggeridge, 2000; Yan et al., 2005). Flood front monitoring is a dynamic monitoring process intended to address these issues mentioned above.

Since the 1960s, many scholars and engineers have carried out extensive experiments and work to monitor the waterflooding front. Currently, the main methods for monitoring flood fronts include microseismic monitoring, numerical simulation, and time-lapse seismic (Wang and Hirsche, 1991; Jupe and Cowles, 1998; Wulff and Mjaaland, 2002; Lekan et al., 2020). In oil and gas field development projects, such as oil and gas recovery, water injection, gas injection and hydraulic fracturing, induced earthquakes have always been a matter of concern. Since 1991, people have applied the experience gained from microseismic monitoring of hydraulic fracturing to the oil and gas field development, which uses inducing microseismics through activities such as oil/gas production, water injection, gas injection and thermal flooding to monitor the progress of the oil and gas field development or related oilfield engineering activities (Wang et al., 1998; Jupe and Cowles, 1998; Jones et al., 2010; Maxwell et al., 2010; Meng et al., 2023). Due to the low cost of microseismic monitoring, it has become the most commonly used technology in the oilfield development monitoring. However, it can only roughly fit and characterize the underground space morphology through a large number of microseismic event points, and can usually only provide approximate results in some monitoring tasks. In addition, due to the low signal-to-noise ratio of the actual on-site received signal and the interference of various noise sources, sometimes many event points irrelevant to the monitoring area are generated, or sometimes no microseismic event points are generated, which limits the application of the method.

Numerical simulation is another method used for waterflooding monitoring and effects evaluation. For homogeneous reservoirs, the Buckley-Leverett equation (B-L equation) can be applied to describe the water injection front at different times (Dullien and Dong, 2002). For low-permeability heterogeneous reservoirs, Li (2006) established a set of waterflooding front measurement methods, and studied interlayer heterogeneity, polymer slugging and other issues. They analyzed the distribution of the remaining oil and provided recommendations for potential development. Zhao et al. (2006) studied the movement law of the waterflooding front in fractured sandstone reservoirs, deduced the analytical expression of the waterflooding curve, and also the change curve of the waterflooding state of the reservoir. On the basis of numerical simulations and physical experiments, Wang et al. (2021) analyzed the movement law of the waterflooding front, established the fundamental method for evaluating the waterflooding development in low permeability reservoirs, and provided a theoretical basis for the accurate assessment of the lead time from the waterflooding front to the production wells. Of course, microseismic monitoring and numerical simulation methods can be used to characterize the dynamics of the waterflooding front. However, they have the drawbacks of a complex solution process and limited accuracy.

In recent decades, time-lapse seismic has become the most effective geophysical method for monitoring subsurface changes during the oil field development process (Fanchi and Pagano, 1999; Cotton et al., 2018; Wang et al., 2021), which has high accuracy. Wang et al. (1998) were the first to utilize time-lapse seismic technology to predict the distribution of remaining reservoirs after carbon dioxide flooding. Wulff and Mjaaland (2002) conducted laboratory experiments to monitor fluid movement and saturation changes by using time-lapse seismic response, which confirmed that time-lapse seismic can effectively monitor fluid migration. Shi et al. (2006) discussed the changes in reservoir physical properties caused by long-term waterflooding and the changes of elastic parameters and seismic response, defined the concept of the waterflooding front, and introduced a method for monitoring based on differential amplitude and singular value analysis. With growing interest in carbon neutralization, some scholars have used time-lapse seismic monitoring technology to observe changes in underground strata injected with carbon dioxide. They monitored the diffusion path of CO_2 injected into deep underground reservoirs, which confirmed that the time-lapse seismic method is the most effective method for monitoring the safety of geological CO_2 storage (Ivanova et al., 2012; White, 2013; Ivandic et al., 2018). Compared with microseismic monitoring, time-lapse seismic monitoring is conducted from the perspective of surface and volume, which can obtain two-dimensional and three-dimensional seismic profiles at different time periods, thereby accurately depicting the areas where changes have occurred underground. However, due to the high cost of time-lapse seismic data, inconsistent acquisition, serious environmental impact, and long acquisition cycle, it is often impossible to achieve long-term continuous monitoring.

With the wide application of node instruments in oil and gas exploration (Zhao et al., 2015; Lei et al., 2018), it has become feasible to continuously collect background noise through passive source seismic methods to carry out long-term continuous monitoring. Unlike microseismic monitoring, the passive source seismic method mainly uses long-term recorded seismic background noise and seismic data processing technology to extract surface wave and body wave records for subsequent imaging. The passive source seismic time-lapse imaging takes into account the characteristics of both microseismic and active source time-lapse seismic, and can achieve continuous and low-cost monitoring from the perspective of imaging. The origin of the passive source method dates back to Aki (1957), who developed an innovative technique, the Spatial Autocorrelation Method (SPAC), to invert the subsurface velocity structure using seismic noise records. Claerbout (1968) demonstrated that the autocorrelation of seismic records coming from the subsurface and received at the free surface of horizontally layered elastic media, is equivalent to their zero offset records, and called this correlation calculation method “daylight imaging”. Subsequently, Rickett and Clairbout (1999) verified Clairbout's theory (Claerbout, 1968) by obtaining a zero offset profile that matched the active source profile through autocorrelation. Schuster and Rickett (2001) processed the virtual shot collection obtained by cross-correlation in the active source imaging process, obtained the image of the underground reflection structure, and renamed the original “solar imaging” to “seismic interference technology”. Bensen et al. (2007) proposed a set of procedures for automatic processing of background noise data. Chamarczuk et al. (2021) systematically summarized various methods and processing strategies for body wave imaging by passive seismic interferometry, providing valuable guidance for subsequent data processing.

To retrieve body waves that are beneficial for seismic background noise imaging, numerous scholars have conducted extensive research (Almagro Vidal et al., 2014; Hartstra et al., 2017; Chamarczuk et al., 2019; Fang et al., 2022). In practical applications, many scholars have verified the feasibility of using passive source data for time-lapse monitoring, and applied it to carbon dioxide geological storage monitoring, mine monitoring, and oil field development (Draganov et al., 2009; Cheraghi et al., 2015; Boullenger et al., 2015; Li et al., 2015; Tsuji et al., 2015; Gu et al., 2021; Liu et al., 2021; Zhang et al., 2022). At present, the cross-correlation superposition method is mainly used in passive seismic data processing (Draganov et al., 2004; Sabra, 2009; Wang

et al., 2016). However, this method usually increases the energy of the related noise several times, which limits the extraction effect of body wave signals. Furthermore, most cases of successful application of passive source seismic methods have been carried out in experimental areas with low levels of background noise and weak changes of underground structures (Xu et al., 2012; Cheraghi et al., 2017; Liu et al., 2021; Chamarczuk et al., 2022). There are fewer reference cases dealing with more complex background noise fields.

In this paper, we propose to integrate the passive seismic method with the time-lapse seismic technology for waterflooding front monitoring, which is not limited to structural imaging. In this sense, we develop a processing and interpretation flow based on similarity analysis of passive source time-lapse images, first considering a theoretical model and then the application to a real case of waterflooding front monitoring in an oilfield. In addition, the variation of the waterflooding front is addressed from a static process to a dynamic process, which provides a new possibility for dynamic monitoring of underground reservoirs in oil fields. The rest of this paper is arranged as follows. Firstly, we briefly introduce the seismic interferometry theory. Next, we describe the data preprocessing and screening procedures and matching analysis methods for data provided by passive seismic. Then, we carry out numerical simulation experiments and data difference enhancement analysis before and after water injection. Finally, we perform time-lapse imaging by processing real passive source seismic monitoring data, and compare the results with those obtained from real monitored production well data.

2. Theory and methods

2.1. Seismic interferometry

The seismic interferometry method (Schuster, 2009; Wapenaar et al., 2010) is the basis for passive source imaging. Assuming that the source is underground, if A and B are two detection points located at positions x_A and x_B, and $S(x_A,t)$ and $S(x_B,t)$ are the seismic records at these two sites, respectively, the reconstructed reflection response in the time domain can be written as:

$$R(x_A,x_B,t)+R(x_A,x_B,-t)=\delta(x_{H,B}-x_{H,A})\delta(t)-S(x_A,t)\otimes S(x_B,-t) \tag{1}$$

where $R(x_A,x_B,t)$ and $R(x_A,x_B,-t)$ are the causal and non-causal parts of the reconstructed reflection response, $x_{H,A}$ and $x_{H,B}$ are the horizontal displacement components at x_A and x_B, δ is unit pulse function, and $\otimes$ represents the interference calculation. At present, the interference algorithms for processing background noise data include cross-correlation, deconvolution, cross-interference and autocorrelation. Here we mainly focus on cross-correlation and autocorrelation operations. The seismic interferometry method applies the cross-correlation technique to extract the Green's function from the background noise recorded by geophones. Assuming that $S(x_A,f)$ and $S(x_B,f)$ are the seismic signals in the frequency domain recorded at the detection points A and B, respectively, the cross-correlation $H(f)$ in the frequency domain is expressed as

$$H(f)=S^*(x_A,f)S(x_B,f) \tag{2}$$

where * represents conjugation and $H(f)$ is the recovered frequency domain data. If $P(f)$ is the source function and $G(x_A,f)$ and $G(x_B,f)$ are the Green's functions, we have

$$S(x_A,f)=P(f)G(x_A,f)S(x_B,f)=P(f)G(x_B,f) \tag{3}$$

Then the cross-correlation can be expressed as

$$H(f)=P(f)^2G(x_A,f)G(x_B,f) \tag{4}$$

When the two selected geophones gradually approach each other and merge at one point, the cross-correlation function becomes the single-channel data autocorrelation function:

$$H(f)=P(f)^2G(x,f)^2 \tag{5}$$

Different from the cross-correlation product that can recover the reflected signals between two geophones, the autocorrelation product can recover the self-excited and received signals at a single geophone through the autocorrelation of noise records coming from underground seismic sources to establish the reflected wave profile. In practical application, due to low SNR, it is difficult to recover virtual shot set records that can be used for subsequent imaging. Therefore, achieving the reflected signal of the subsurface wavefield by using background noise autocorrelation is a great complement to passive source seismic interference imaging. Here we will use the autocorrelation method in the subsequent processing of profile images.

2.2. Data preprocessing and screening procedures

Accurately reconstructing the empirical Green's function from long-term noise data requires a series of complex operations. The processing flow of the seismic interferometry-based passive source method (Bensen et al., 2007) involves data preprocessing (average removal, trend removal, resampling, bad track removal, band-pass filtering, time window segmentation, time domain normalization and spectral whitening), interferometry processing and time domain stacking. Among them, preprocessing operations are an important step to improve the quality of stacking results. By segmenting long-duration noise records and stacking them, the imaging effect can be significantly improved. But for the segments with poor quality, due to their continuous overlap, not only the imaging effect will be reduced, but also the weak body wave signal will be submerged in noise. Therefore, it is necessary to screen the data when processing.

During water and gas injection processes in an oil field, due to mechanical vibration, vehicle movement and human activity on the surface of the work area, the collected signals contain a large amount of useless noise and the body wave signal used for imaging is extremely weak. Except for industrial interference, linear interference and harmonic interference, most of the noise energy is recorded in the form of a surface wave and overlaps with the frequency band of the body wave signal. The remaining noise is relatively easy to remove, but directly removing surface wave interference will remove the existing weak body wave signal, which is time-consuming and meaningless to process for each data segment. The illumination diagnostic method is an effective method for identifying body wave signals generated from the subsurface, which is mainly based on the difference in the propagation speed of body waves and surface waves in the study area. It determines whether the relevant noise panel is dominated by body waves by setting the limit of the slowness parameter. The illumination characteristics of transient sources can be studied by the correlated common source panel C^S, which can be described as

$$C^S(x_B,x_A,t)=\frac{1}{\rho c}\left(\mu^{obs}(x_A,x_S,-t)*\mu^{obs}(x_B,x_S,t)\right) \tag{6}$$

It is as if a source located at receiver x_A emits energy to multiple

receivers x_B within a finite angular window. In this last expression ρ and c are the constant mass density and velocity of the medium at and outside the boundary ∂D, respectively, $\mu^{obs}(x_A, x_S, -t)$ is the time reversal wavefield observed at x_S from the transient source at x_A, and * represents convolution in the time domain. In this panel, information about the illumination characteristics of the specific source x_A at the boundary ∂D is provided by the event at time $t = 0$ and the position of the virtual source. The collection of these events is called virtual source function (van der Neut et al., 2011). Then, we use the slant-stack transform of field v, described by $v(p,\tau) = \int \widetilde{v(x,\tau+px)}dx$, where p is the ray parameter, x is the offset, and τ is the intercept time at $p = 0$. Next, we evaluate the slant stack at $\tau = 0$ for each virtual common-source panel C^S:

$$\tilde{C}^S(x_A, p) = \int C^S[x_B, x_A, p \cdot (x_B - x_A)]dx_B \tag{7}$$

where C^S is the representation of the virtual-source function of the transient source S in the $\tau - p$ domain. The $\tilde{C}^S$ describes the dominant ray-parameter contribution from the transient source to the virtual source located at x_A and recorded at x_B. The discriminant criterion can be defined as

$$C^S(x_B, x_A, t) = \begin{cases} 0, & \text{if } \max\left(\left\|\tilde{C}^S(x_A, p)\right\|\right) > p_{limit} \\ \frac{1}{\rho c}\left(\mu^{obs}(x_A, x_S, -t) * \mu^{obs}(x_B, x_S, t)\right), & \text{if } \max\left(\left\|\tilde{C}^S(x_A, p)\right\|\right) < p_{limit} \end{cases} \tag{8}$$

where $\max(\left\|\tilde{C}^S(x_A, p)\right\|$ is the dominant ray-parameter value, and p_{limit} is the minimum expected value of the P-wave slowness in the recording area. More details about the illumination diagnosis procedure can be found in Almagro Vidal et al. (2014).

2.3. Matching analysis of time-lapse seismic data

As in the case of active source time-lapse seismic imaging, after completing passive data preprocessing and data screening, in order to highlight the changes in the underground reservoirs and eliminate the non-repeated acquisition factors in the time-lapse seismic, there is to do the matching analysis (mutual averaging processing) of the imaging data for different time periods (Guo et al., 2012). For this, multiple correction operators are used to match and correct differences in seismic data at different times, including time correction, amplitude equalization, phase correction, and matched filtering. Generally, for two different sets of data (corresponding to different time periods), we first select data in a time window as the basic data based on the non-reservoir segment of the first data. Then, in this time window, the basic data is matched as closely as possible with the second data to calculate the best matching filter F_{match}. Finally, this filter is applied to the reservoir data of interest (monitoring data) in the second data to highlight the changes in the reservoir and achieve the purpose of monitoring. Let S_{basic1}, S_{basic2}, Y_{origin}, Y_{filter} be the first period basic data of non-reservoir segment, the second period data of non-reservoir segment, the second period reservoir data before correction, and the second period reservoir data after correction in the time domain, respectively, then

$$S_{basic2} = S_{basic1} * F_{match}, Y_{filter} = Y_{origin} * F_{match} \tag{9}$$

Therefore, it is crucial to construct the best matched filter using S_{basic1} and S_{basic2}, which can be obtained by the following four operators:

$$F_{match} = F_t * F_p * F_{amp} * F_m \tag{10}$$

where * means convolution in the time domain. The time shift correction operator F_t can calculate the time corresponding to the peak value of the cross-correlation function by performing cross-correlation operations on the S_{basic1} and S_{basic2}, that is, the relative time delay of the two sets of data. The phase correction operator F_p can be obtained by performing phase scanning on S_{basic2} based on S_{basic1} and selecting the phase angle corresponding to the maximum value of the correlation coefficient between the two measurement lines. The amplitude correction operator F_{amp} can be obtained by calculating the root mean square (RMS) amplitude of each trace of the S_{basic1} and the S_{basic2}, respectively. The matched filter operator F_m can be obtained from the Wiener filter equation. For more detailed calculation process of the above operators, readers can refer to Guo et al. (2012). In order to obtain better matching results, we usually need to perform multiple matching analysis processes. Since our goal is to minimize the differences between non-target layer data, the matching analysis can be terminated when the errors between non-target layer data are not significantly reduced. The specific number of times depends on the specific situation.

3. Laboratory experiment

3.1. Models, synthetic data and results

To verify the feasibility of the passive source imaging time-lapse monitoring, we simulate the process before and after water flooding in the oil field using the seismic wavefield simulation method. During the process of injecting water into the underground, water will force out oil and gas from the pores of the reservoir rocks, which will change the seismic velocity regime in the underground reservoir (water injection layer). Therefore, based on the original velocity model, we will obtain new models by modifying the velocity after water injection. As shown in Fig. 1, we start from four velocity models in which the reservoir burial depth is about 1250 m, the water injection front range is 0–600 m, the reduction speeds before and after water injection are different in the four models, and the positions of the water injection front are also different. The receivers are located on the surface with a spacing of 20 m. To better simulate the real subsurface conditions, more than 200 seismic sources are distributed around the injection positions (50–70 sources), the bottom (150 sources) of the model and the surface (15 sources). These sources are used to simulate passive source data, among which the surface sources are mainly used to generate surface wave noise (which is consistent with actual acquisition conditions). The two-dimensional seismic

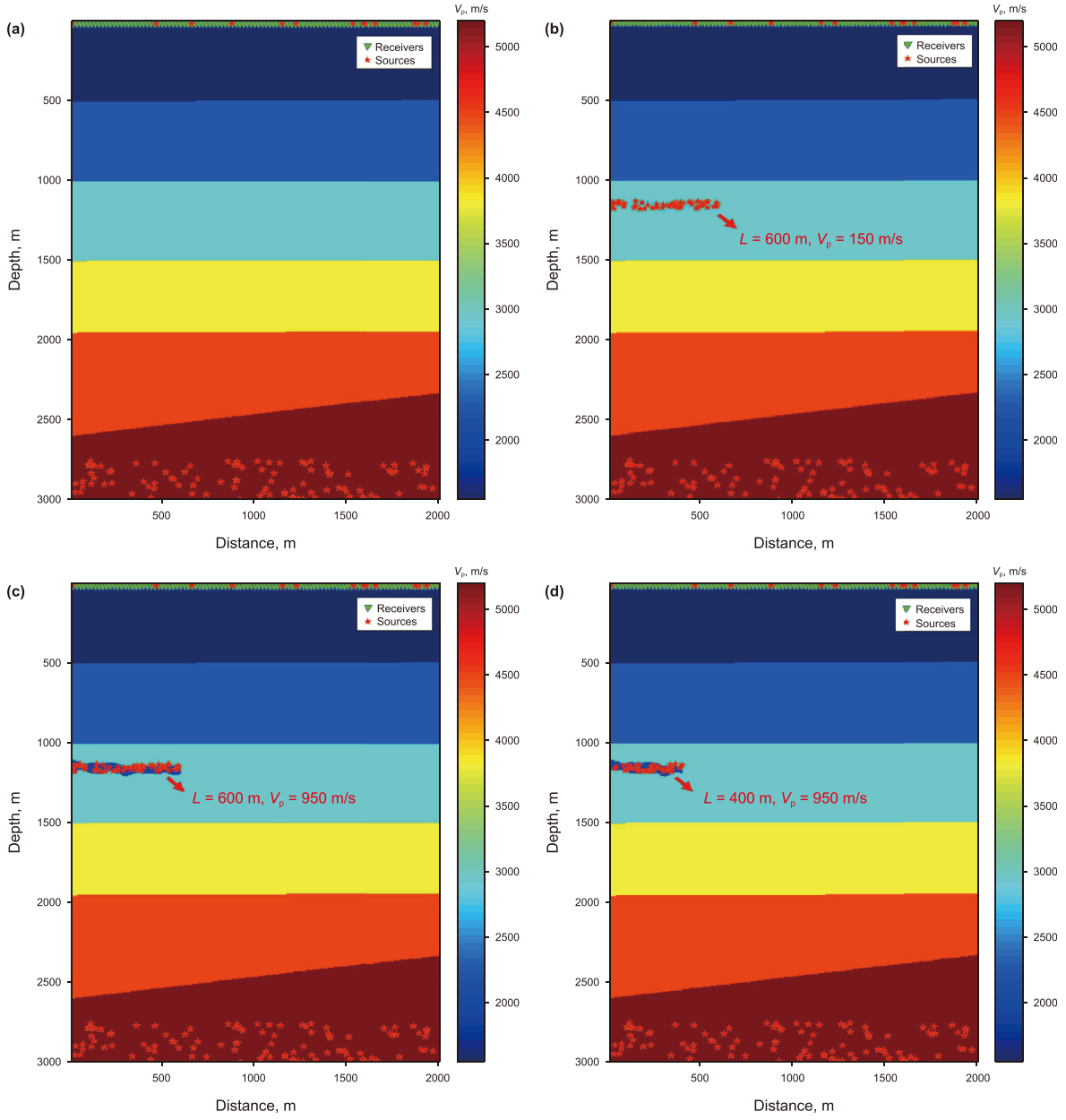

Fig. 1. Theoretical velocity models: **(a)** before water injection; **(b)** with water injection range of 0–600 m and reduction speed of 150 m/s; **(c)** with water injection range of 0–600 m and reduction speed of 950 m/s; **(d)** with water injection range of 0–400 m and reduction speed of 950 m/s. Red stars represent sources and green inverted triangles are receivers.

records are simulated using finite differences elastic wave filed simulation (Lan and Zhang, 2011), and single-component data are taken for the experiment with a sampling interval of 2 ms.

In order to compare with the virtual shot records constructed by passive sources, we first excite a source at the first receiver position of the model in Fig. 1(a)–(d) and obtain the active source shot records shown in Fig. 2(a)–(d). By comparing the active seismic shot records with different velocity regimes after water injection, it can be clearly observed that a new reflection event appears at about 1.2 s. This is due to the strong reflection coefficient generated by the decrease in formation speed. The greater the reduction speed, the more obvious the difference will be in the seismic record. The location of the new reflection event is consistent with the designed water injection model. At the same time, decreasing the velocity will cause the reflection event from the underlying layer to change phase, and the same phase event will not be able to align before and after the speed change. Then, we simulate a passive source seismic record with duration of 20 min through the passive source observation system, and divided it into 5 s segments. The passive source virtual shot records obtained after a series of data processing and passive source interference processing are shown in Fig. 3(a)–(d). The data preprocessing includes de-mean and de-trend, resampling, bandpass filtering, time splitting, time-domain normalization, spectrum whitening, data screening, cross-correlation interference processing and time-domain stacking. By comparing the passive source seismic records with different velocity regimes after liquid injection, we can see that the results are consistent with the active source seismic records. Again, a new reflection event appears at about 1.2 s.

Then, to better compare the profile changes before and after gas injection, we show the zero-offset imaging profile of the active source through the excitation at the receivers position and the

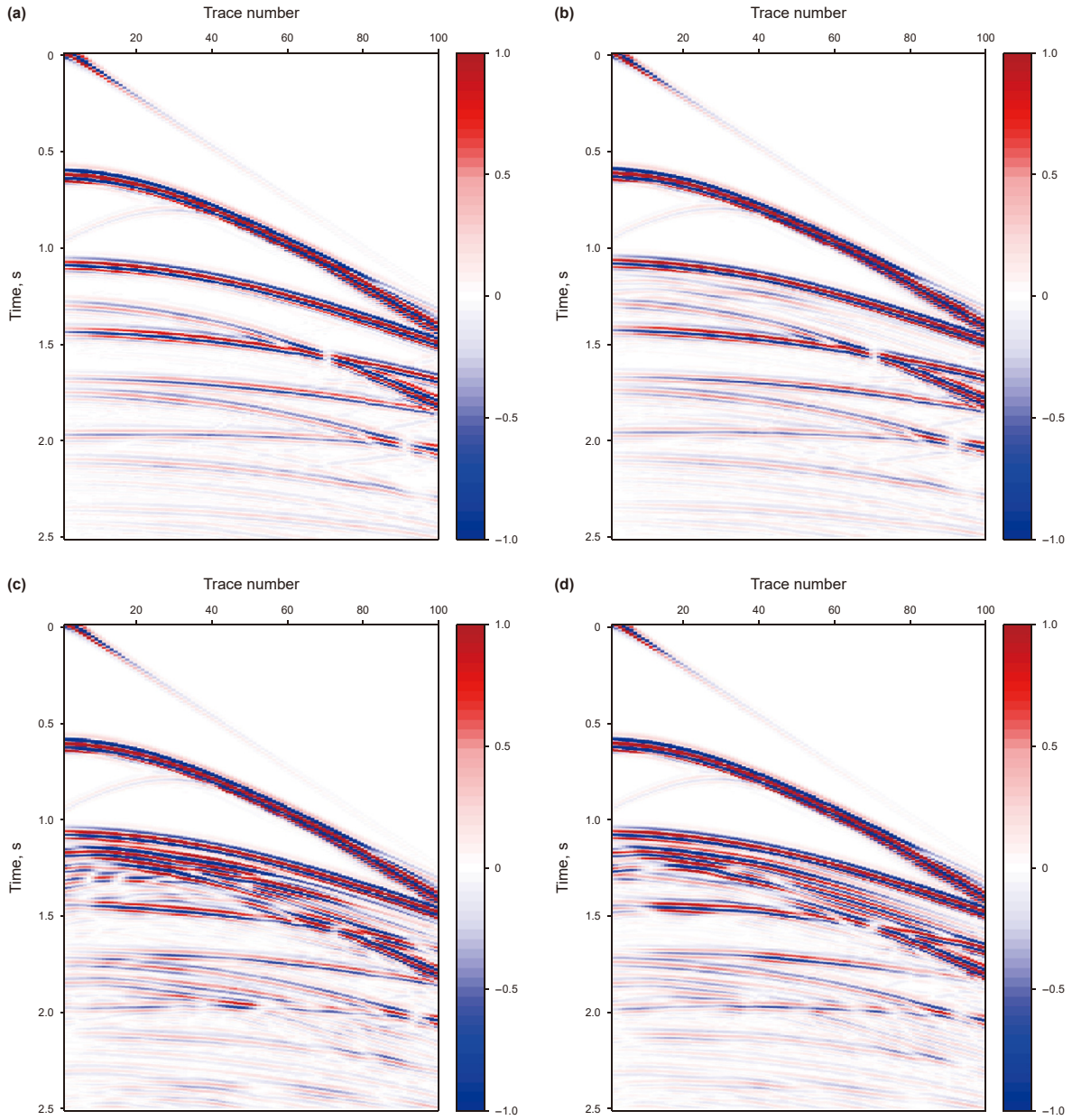

Fig. 2. Active source shot records: **(a)** before water injection; **(b)** water injection range 0–600 m, reduction speed 150 m/s; **(c)** water injection range 0–600 m, reduction speed 950 m/s; **(d)** water injection range 0–400 m, reduction speed 950 m/s.

reception at the receivers position (Fig. 4(a)–(d)), and the correlation profile of the passive source through autocorrelation and stacking (Fig. 5(a)–(d)), respectively. It is easy to see that the passive source correlation profile is more consistent with the active source zero-offset imaging profile, and that the time and location of the anomaly correlate basically in all cases. The new event appearing near 1.2 s is associate with the position of the velocity anomaly designed in the water injection model, and can reflect the changes in the reservoir before and after waterflooding. Finally, to better highlight and monitor the changes in the target layer, we carry out a normalized treatment for the active source profiles and the passive source autocorrelation profiles before and after water injection (reduction speed 950 m/s), and display them according to the geophone arrangement in Fig. 6(a)–(d). Since seismic records are both positive values and negative values, we use the maximum and minimum normalization method to normalize them to the range of −1~1:

$$\bar{x} = 2 \times \frac{x - \min(x)}{\max(x) - \min(x)} - 1 \tag{11}$$

$\bar{x}$ here represents normalized data and x represents original data. It can be clearly observed that the seismic event of the target layer is staggered, and that the seismic events above the target layer have good continuity. It can be inferred that the formation in this section has undergone drastic changes, which provides a basis for monitoring changes in the reservoir.

3.2. Similarity analysis

Generally, the quality of data obtained in actual production is poor, and the target formation is buried deep, so autocorrelation

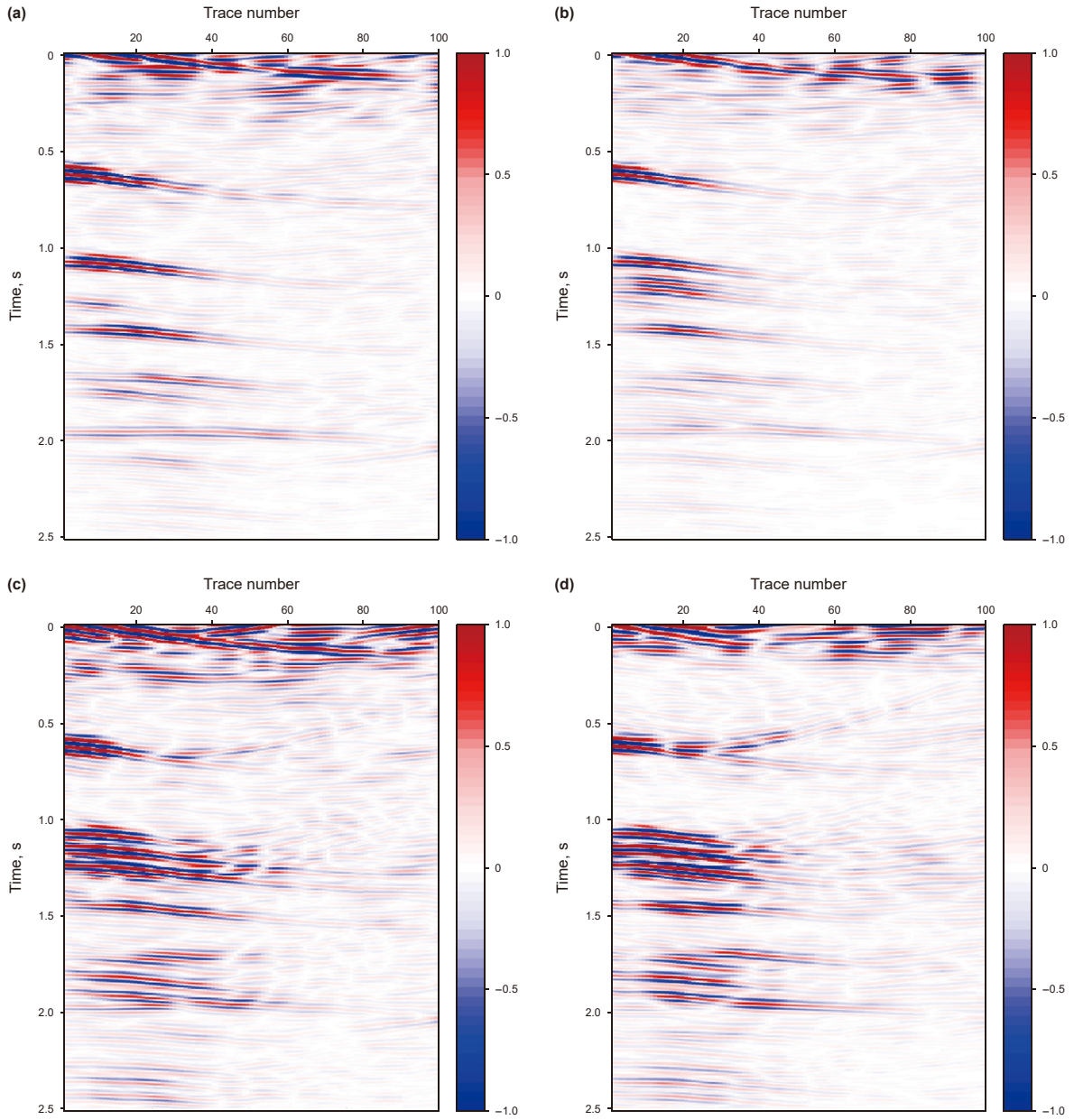

Fig. 3. Passive source virtual shot records: **(a)** before water injection; **(b)** water injection range 0–600 m, reduction speed 150 m/s; **(c)** water injection range 0–600 m, reduction speed 950 m/s; **(d)** water injection range 0–400 m, reduction speed 950 m/s.

imaging is mainly adopted. The purpose of this paper is not to obtain structural images, but to reflect the difference between time-lapse seismic images with a view to monitoring the water-flooding front. Since the actual passive-source body-wave data coming from deep formations usually have a low frequency, to better show the movement of the waterflooding front, eliminate other interferences, and highlight image differences, we carry out F-X filtering and low-pass filtering (frequency band range: 8–12 Hz) of the imaging data shown in Fig. 6(a)–(d). The results for comparison are shown in Fig. 7(a)–(d) where the imaging data in the areas within the blue boxes have obviously changed, and the imaging data out the blue boxes remain basically unchanged. After the above processing, the cut-off surface of active source imaging is basically the same as the cut-off surface of the waterflooding front, and the interface of passive source imaging is slightly different from the cut-off surface of the waterflooding front (which will be affected by manual interpretation); but both can reflect the migration of the waterflooding front, thus achieving the dynamic monitoring of the flood front. For those engaged in geophysics, the imaging results shown in Fig. 7(a)–(d) are sufficient to explain the changes of the waterflooding front, but not so for engineers dedicated to work in oil field, for whom it will be difficult to understand the differences between seismic data and the results will be affected by the subjective manual interpretation.

With the purpose of obtaining a more accurate and direct waterflooding front imaging, we propose a simple similarity matrix analysis. Assuming that $X = [x_1, x_2, \cdots, x_n]$ and $Y = [y_1, y_2, \cdots, y_n]$ are the processed imaging data before and after water injection, respectively, the correlation coefficient of the imaging data at the same geophone before and after water injection is expressed as

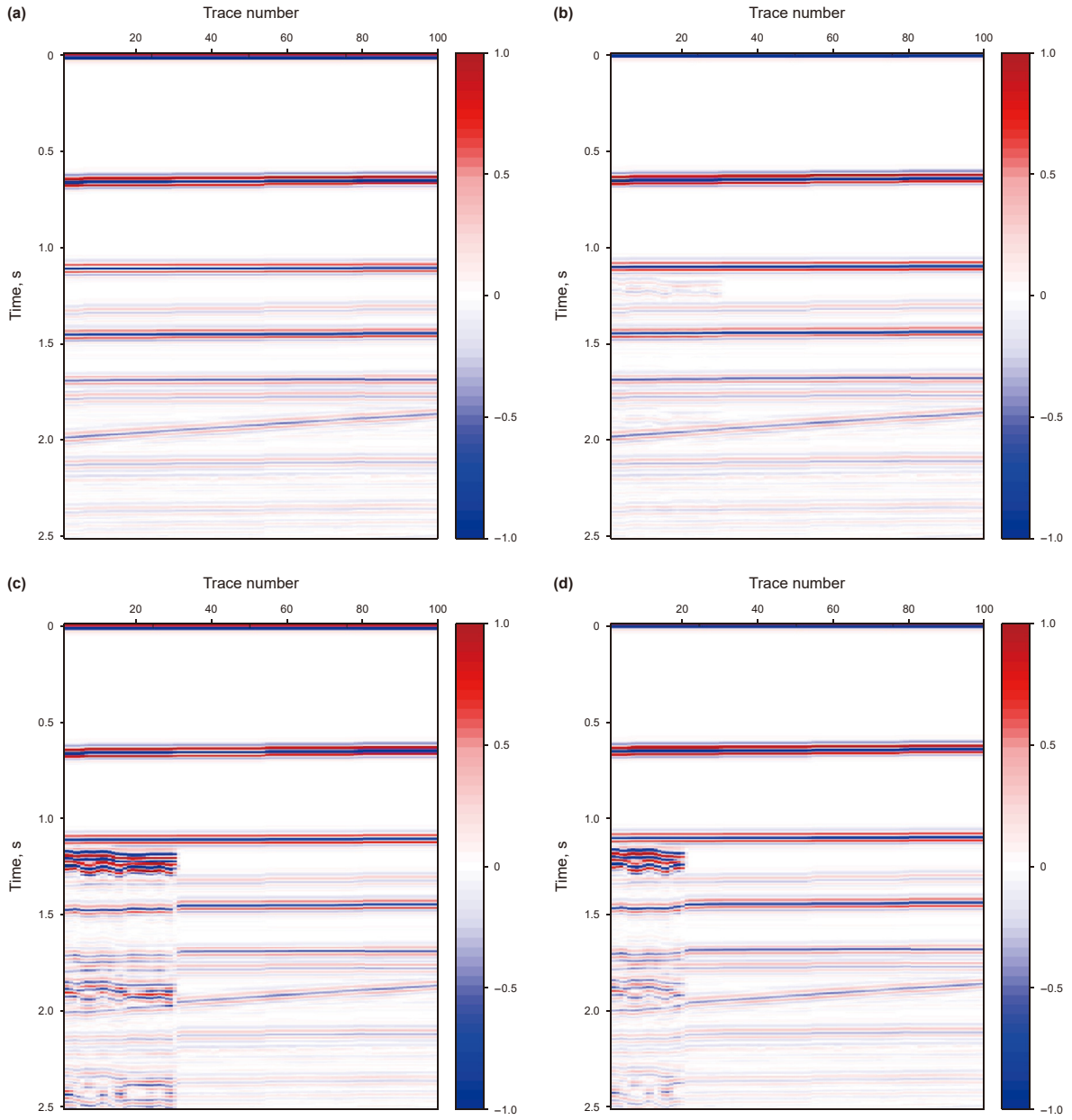

Fig. 4. Active source zero-offset imaging profiles: **(a)** before water injection; **(b)** water injection range 0–600 m, reduction speed 150 m/s; **(c)** water injection range 0–600 m, reduction speed 950 m/s; **(d)** water injection range 0–400 m, reduction speed 950 m/s.

$$C = [c_1, c_2, \cdots c_n] = \mathrm{corr}(x_i, y_i) \tag{11}$$

where C are the mentioned correlation coefficients, $c_1, c_2, \cdots c_n$ are the correlation coefficients calculated for data at different geophones, corr denotes the correlation function, and i refers to the i-th geophone. From the one-dimensional vector C the similarity matrix M can be formulated as

$$M = \mathrm{repmat}(C) = \begin{bmatrix} c_1, c_2, \cdots c_n \\ \cdots\cdots\cdots \\ c_1, c_2, \cdots c_n \end{bmatrix} \tag{13}$$

where repmat is the matrix extension operator. To facilitate readers' understanding, we expand the dimension of M to be the same size as the imaging data, and thus the coordinates of M are consistent with the seismic imaging data handled in this paper. Fig. 8 shows the results provided by the similarity matrix analysis. The area containing small values is the abnormal imaging area and the imaging interface (dividing vertical straight line in the illustration) is very obvious. The abnormal imaging interfaces generated from the active source and passive source processes are basically consistent with the position of the actual designed waterflooding front, which can intuitively reflect the cut-off surface of the waterflooding front (the black line in Fig. 8(a)–(d)), improve the monitoring accuracy and therefore the final result. Experimental results with synthetic data demonstrate that it is feasible to use passive source time-lapse imaging for waterflood front monitoring. As an aid to the reader, in Fig. 9 we show the flowchart for processing and interpretation of passive source time-lapse images for flood front monitoring.

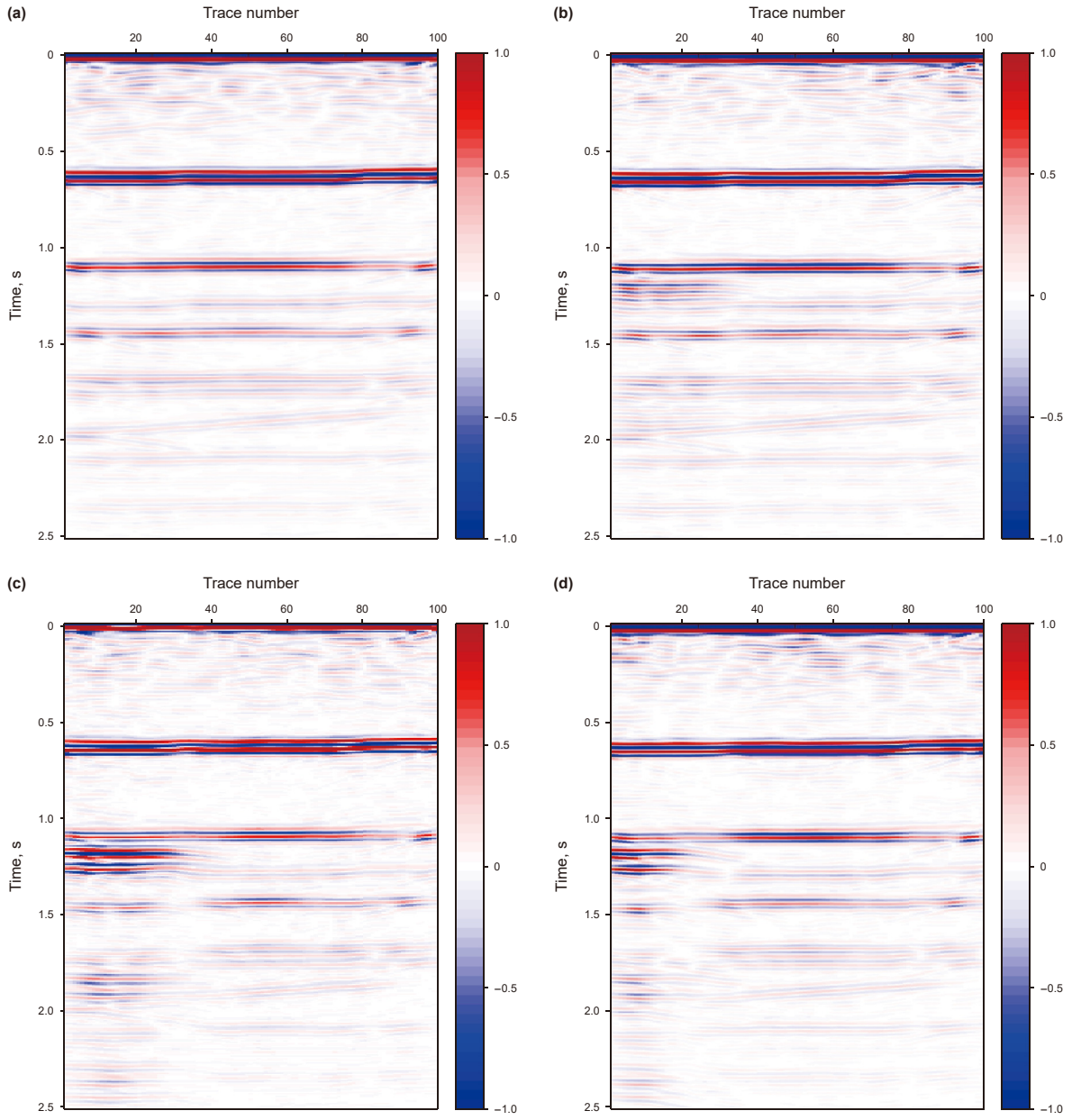

Fig. 5. Passive source imaging profiles: **(a)** before water injection; **(b)** water injection range 0–600 m, reduction speed 150 m/s; **(c)** water injection range 0–600 m, reduction speed 950 m/s; **(d)** water injection range 0–400 m, reduction speed 950 m/s.

4. Test with real data

4.1. Field data set and results

In order to verify the viability of the proposed method and the advantages of its application, background noise data were collected during the pressure flooding process in a working area of Shengli Oilfield in China, where the reservoir depth is about 3000–3300 m, which corresponds to a time of about 2.5 s in the seismic profile, as shown in Fig. 10. The pressure flooding process in the X46 water injection well was monitored by the long-term passive source observation system to study and analyze the changes in the underground reservoirs in the other five production wells before and after pressure flooding. As shown in Fig. 11, the observation system resembles a star layout. The monitoring geophones are deployed on the bottom horizontal plane projection of the X46 water injection well and are arranged between the bottom horizontal plane projections of each production well, with an envelope radius of 400–500 m. The vibration itself caused by the water flooding process has a huge energy difference and the frequency band range of the signals is wide. Obtaining images of the underground reservoir with the help of these signals and further analyze the change of the water flood front requires continuously collecting the vibration signals for a long time. In this project, we select Smartsolo high-resolution single-component intelligent seismic sensor IGU-16HR (more details about the geophones, please visit https://www.smartsolo.com.cn/cp-2.html), which can work continuously for 35 days at 1 ms sampling. The node instrument was not charged during the entire collection period. The project lasted 32 days from the start of water injection to the stop during this phase of our monitoring, so a total of 32 days of data were collected. When processing actual data, in order to improve computing efficiency,

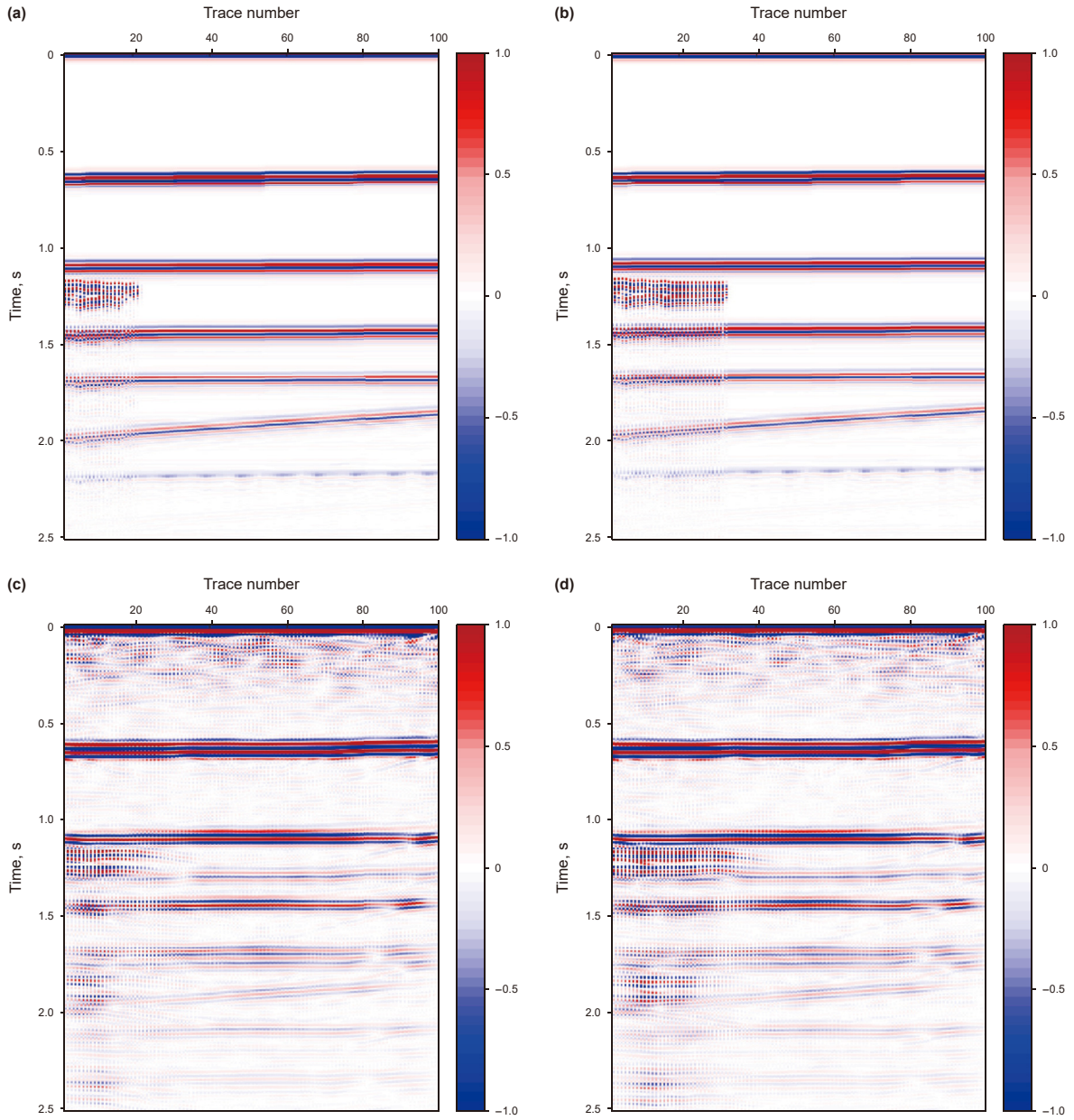

Fig. 6. Comparison of images before and after water injection: comparison of zero-offset images before water injection and for a water injection range of 0–400 m **(a)** and 0–600 m **(b)**; comparison of passive source images before water injection and for a water injection range of 0–400 m **(c)** and 0–600 m **(d)**.

the collected raw data was resampled from 1 ms to 2 ms.

During the process of water injection and oil production, strong mechanical noise and strong surface wave interference will be generated on the surface. For this reason, we first undertake the data screening and analysis processes due to the strong impact of surface noise on the monitoring data. The screening method adopts the illumination diagnosis method introduced above. Fig. 12 shows the typical actual seismic records of different qualities at different time periods after data screening. In Fig. 12(a) and (b), the overall signal distribution is regular, and the signal amplitude at each detector is quite different, which is obviously greatly influenced by the ground conditions because a large amount of random noise and ground vibration signals are involved, and the quality are poor. In contrast, the signal distribution in Fig. 12(c) and (d) is consistent with the characteristics of signals propagating from the subsurface, and the signal amplitude at each geophone is stable because it contains more effective body wave signals, and the quality is good.

A total of 32 days of background noise data were collected for underground reservoir monitoring, and the original datasets were processed and interpreted following the flowchart shown in Fig. 9. To reach this goal, we used the passive source time-lapse monitoring method, and thus obtained images every 10 days from the beginning of monitoring. Two days of data were used for each imaging session, and a total of four imaging sessions were performed. Fig. 13 allows the comparison of the passive source time-lapse imaging results from two days before the start of the pressure drive project (July 20 to 21) until days 11 and 12 of the project (July 30 to 31), where the horizontal axis represents the geophone number and the vertical axis is the zero-offset travel time. Fig. 14 directly compares and analyzes the imaging results at each receiver point at different time periods.

By putting together data at different times at the same receiver

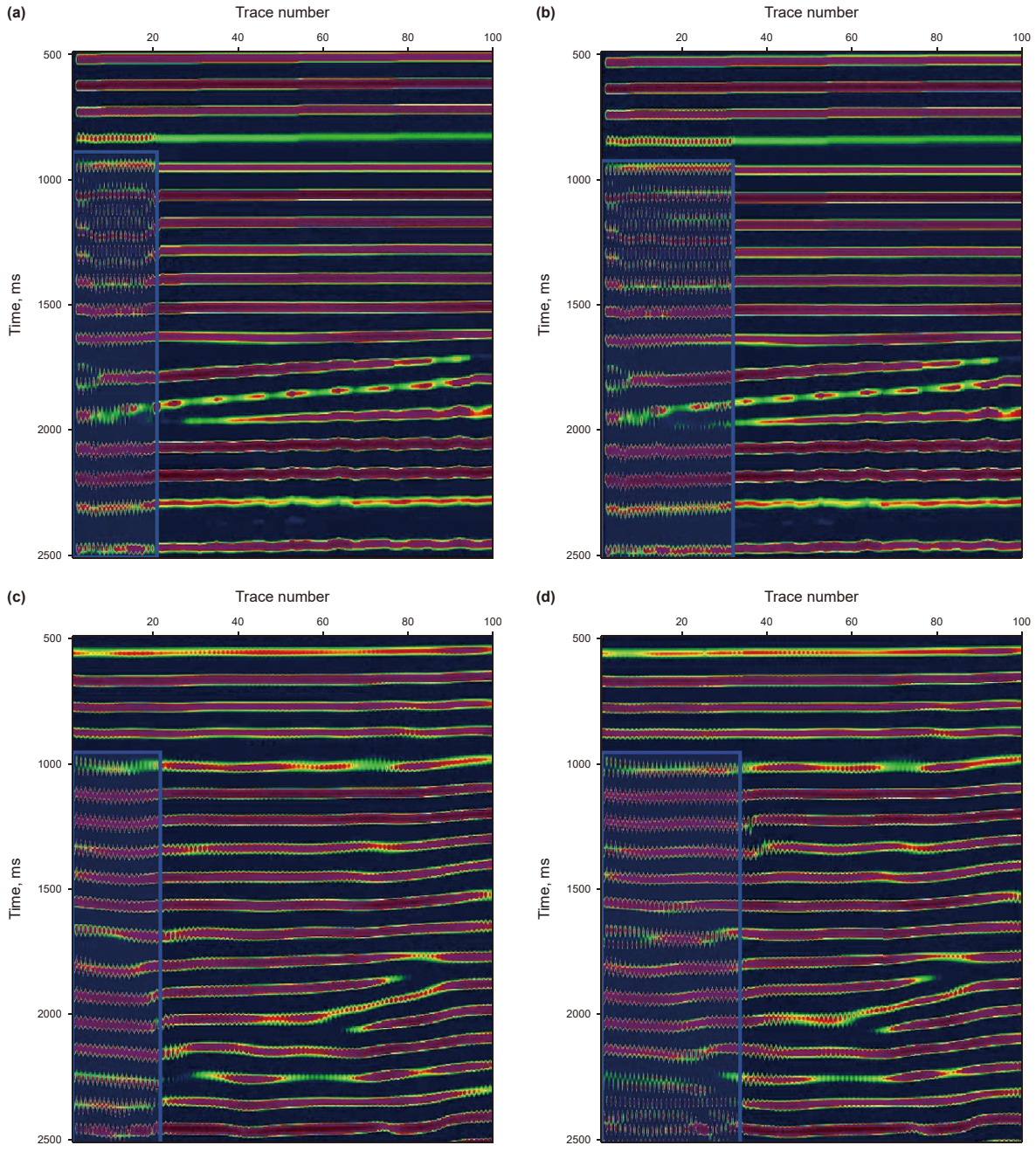

Fig. 7. Comparison of images after F-X filtering and low-pass filtering: comparison of zero-offset images before water injection and for a water injection range of 0–400 m **(a)** and 0–600 m **(b)**; comparison of passive source images before water injection and for a water injection range of 0–400 m **(c)** and 0–600 m **(d)**.

point and analyzing the consistency of the signal, we can understand the characteristics of changes that occur in the reservoirs. The areas within the blue boxes are those with obvious differences in the data. It can be clearly observed that the monitoring data before and after water injections in Well X41 and Well X42 are quite different: in the underground reservoir of Well X41 there are obvious changes, but the abnormal range of the seismic response is not as large as that of Well X42. There is still some distance between the flood front and the bottom of Well X41, which is interpreted as a connected fracture in the subsurface, but which has not yet completely penetrated. Pressure flooding has a great impact on the underground reservoir of Well X42, and the difference before and after monitoring is the largest, and the subsoil is basically connected, so it is likely to be penetrated. Pressure flooding in Well X26 and Well X45 has an impact on these underground reservoirs, but the seismic response is much lower than that of Well X41 and Well X42, indicating that the subsoil has been affected by pressure flooding. However, pressure flooding in Well X26 and Well X45 is much less obvious than in Well X41 and Well X42. That means that the reservoir along Well X41 and Well X42 has changed, but there are no solid signs of connectivity. The pressure flooding effect in Well X47 is not obvious, and the imaging results show that there are no obvious changes in the reservoir near the water injection well, and the waterflooding front is far from the bottom of Well X47.

Following the same interpretation method, the differences between images will increase when changes occur in the

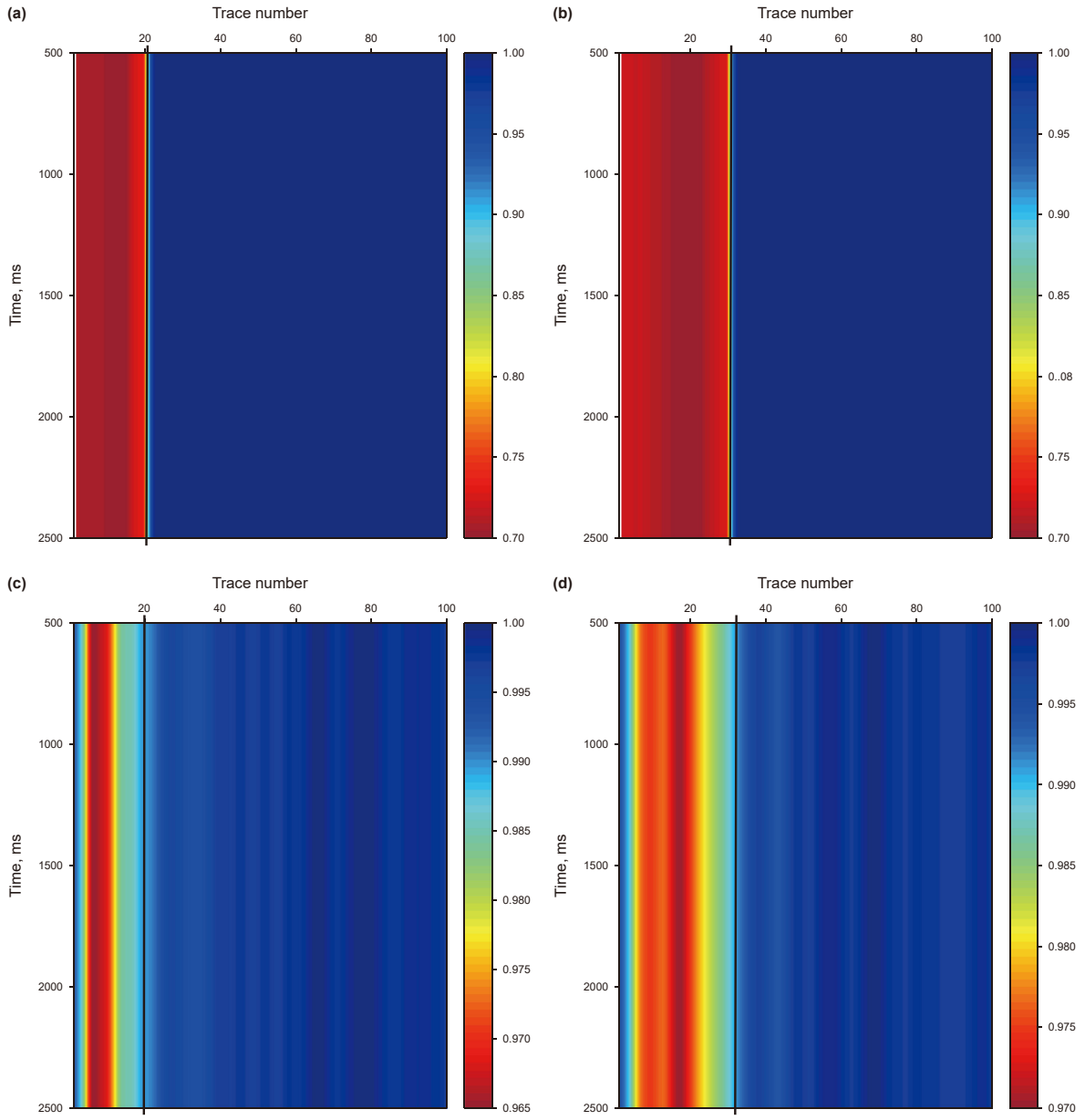

Fig. 8. Similarity matrix results: zero-offset images before water injection and with a water injection range of 0–400 m **(a)** and 0–600 m **(b)**; passive source images before water injection and with a water injection range of 0–400 m **(c)** and 0–600 m **(d)**. (The black line is the dividing line of the abnormal area, which can be understood as the cutting edge of the waterflooding front.)

underground reservoirs. Next, we consider the passive source time-lapse imaging results from the days 21st and 22nd (August 10–11) and then the days 31st and 32nd (August 19–20). As can be seen in Fig. 15, with the continuous pressure flooding, the reservoir in Well X41 is still changing obviously, and the difference continues to increase. The underground fracture is basically connected and is very likely to have been penetrated. The reservoir in Well X42 is still changing intensely, which is explained by the fact that the reservoir is in a relatively stable state after fracture penetration. With the continuous pressure flooding in Well X26 and Well X45, the imaging difference gradually increases and the waterflooding front continues to advance to the bottom of the well. The monitoring results of Well X47 show that the pressure flooding effect is average, and the reservoir near the well presents obvious changes, but they are far from its bottom. Looking at Fig. 16, the imaging difference between Well X41 and Well X42 persists, which is explained by the fact that the underground reservoir is relatively stable after fracture penetration. The monitoring results of Well X26, Well X45 and Well X47 show that the pressure flooding is in progress, and the difference continues to increase and still has an impact on these wells. The change in the reservoir in Well X26 is the largest, while the reservoir in Well X47 has the smallest change. The change in the reservoir in Well X45 is weaker than that in Well X26.

To obtain an accurate estimation of the flood front, we carry out similarity matrix calculation using the time-lapse image results shown in Figs. 14–16, and we obtain the normalized (the range of 0–1) similarity matrix results (Fig. 17(a)–(c)). It can be seen that the

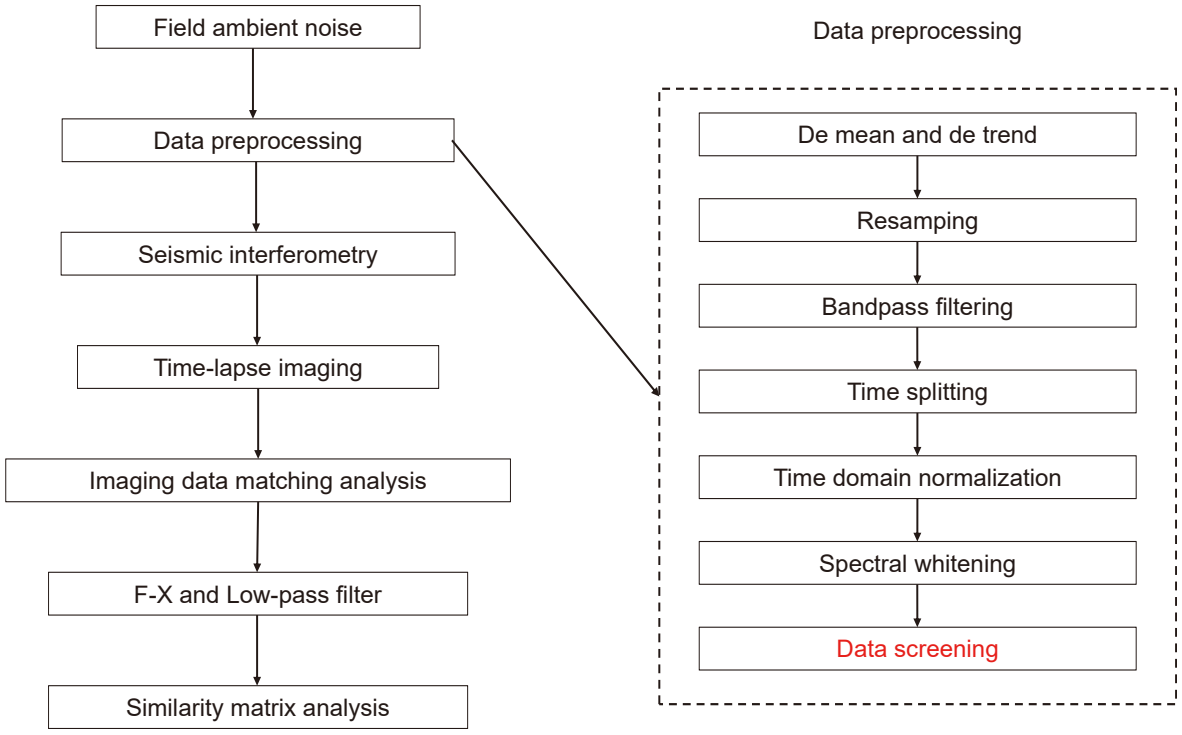

Fig. 9. Flowchart for processing and interpretation of passive source time-lapse images for waterflooding front monitoring.

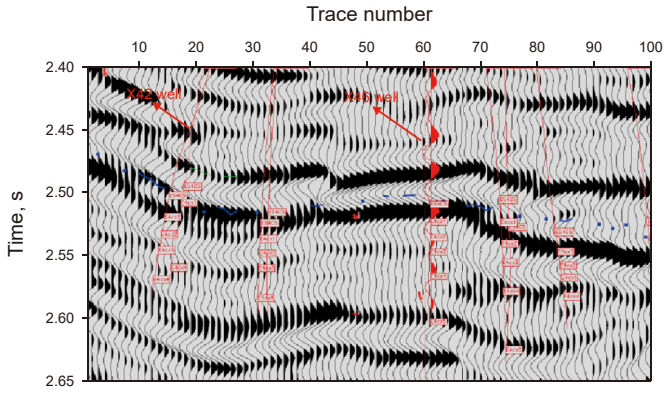

Fig. 10. Active source seismic profile through wells in the monitoring area (The remaining three wells are not on this seismic profile).

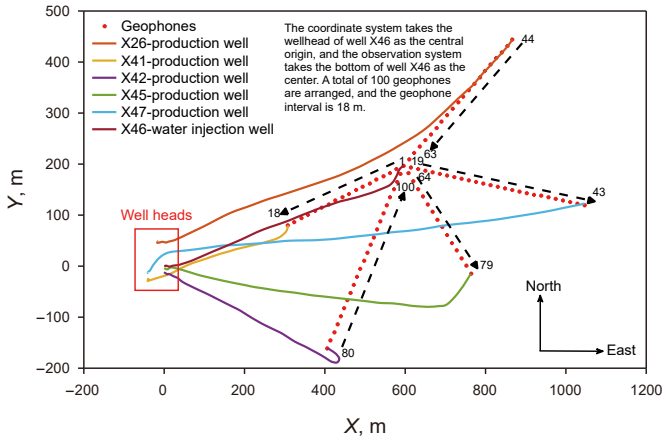

Fig. 11. Observation system resembling a star layout (The black numbers and black dotted lines are the geophones numbers and layout directions.)

similarity of the results gradually decreases as the pressure flooding progresses. Based on the results shown in Fig. 17(a)–(c), by projecting the position of the black line that marks the anomaly boundary onto the corresponding geophone position in the observation system, we can draw the underground waterflooding fronts predicted by the passive source imaging method for three different time periods (Fig. 18(a)–(c)), and thus observe their progress over time (see colored irregular area). The red arrows represent the level of predicted underground connectivity. The thicker the arrow, the better the connectivity effect. Red lines represent fracture directions. According to the fracture distribution plotted in Fig. 19(a)–(e), Well X41 and Well X42 are directly penetrated by the fractures, which means that they are connected by natural fractures during the pressure flooding. Looking at the map of the working area (lower left corner), we can see that several large fractures are distributed along Well X46, Well X41 and Well X42, which is consistent with the actual monitoring prediction results. The fractures distributed near Well X26 are perpendicular to the well trajectory and the underground fractures are connected in the initial stage of pressure flooding, so the impact on production is limited. Nevertheless, as the pressure flooding surface approaches the bottom of Well X26 in the later stage, the pressure drive effect improves rapidly. The fractures and well trajectory near Well X45 have a basically horizontal layout, and it is easy to achieve the production increase effect with pressure flooding, but the production increase is limited. The fracture distribution near Well X47 is oblique to the well trajectory; therefore, if pressure flooding is increased, there should have a better effect on underground connectivity and increase production.

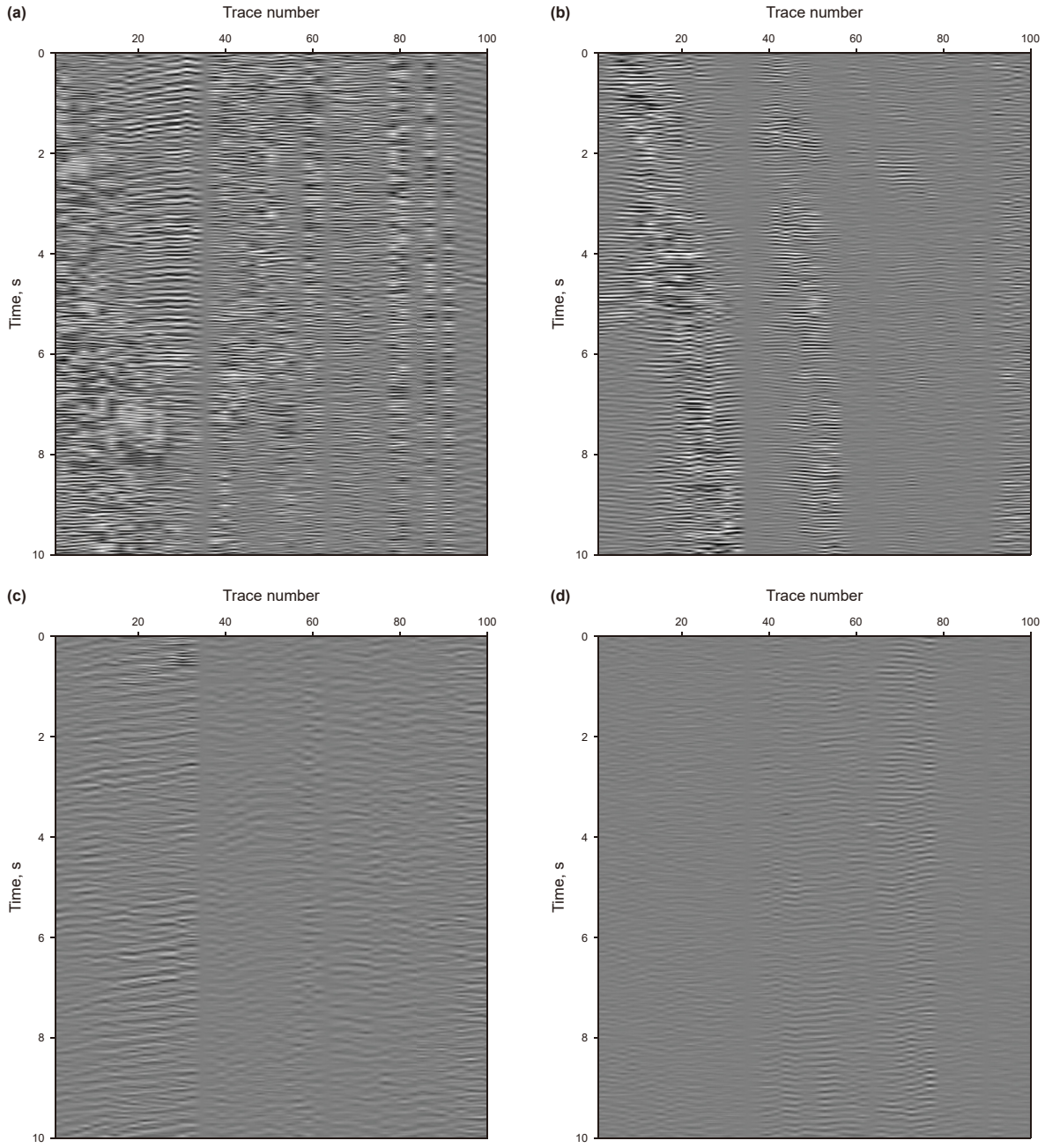

Fig. 12. Actual seismic records after data screening: **(a)**–**(b)** poor quality time segments; **(c)**–**(d)** good quality time segments.

4.2. Tracking and checking results

In this pressure flooding monitoring, we use background noise data collected over 32 days, from July 20 to August 20. From these data, we conduct the passive source seismic imaging process for four time periods, namely: July 20 to July 21, July 30 to July 31, August 10 to August 11 and August 19 to August 20. The results show that the order of connectivity effects of the five wells after pressure flooding is as follows: X42, X41, X45, X26 and X47. In comparison, Well X47 has the smallest reservoir change among all wells, which means that the water flood is advancing under the pressure impulse, but the resistance is great. Therefore, pressure flooding operation can be further implemented in this well. Obviously, production is expected to increase with the advance of the flood front.

Fig. 19 shows the in-situ production data of the five oil wells monitored in the target area for the purpose of tracking and verifying the results after pressure flooding work. Well X26 (Fig. 19(a)) had an obvious pressure flooding effect, and the water content reached a peak of 55.6% on August 12. After stopping the pressure flooding operation, oil production increased obviously and reached its peak on August 15. Regarding Well X47 (Fig. 19(b)), the fluctuation of oil and gas production is not obvious during the pressure flooding operation, indicating that the pressure flooding effect is not clear. The water content suddenly increased on August 4, followed by a significant increase in oil and gas production, indicating that pressure flooding played an effective role, especially after that date. After stopping the pressure flooding operation, oil production

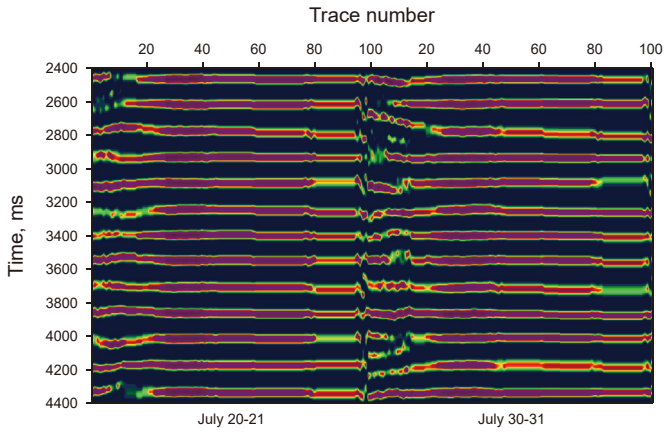

Fig. 13. Time-lapse imaging results of background noise data (July 20–July 31). The horizontal axis represents the trace number or geophone number and the vertical axis is the zero-offset travel time (The 100 traces on the right are data from July 20– July 21, the 100 traces on the left are data from July 30– July 31.)

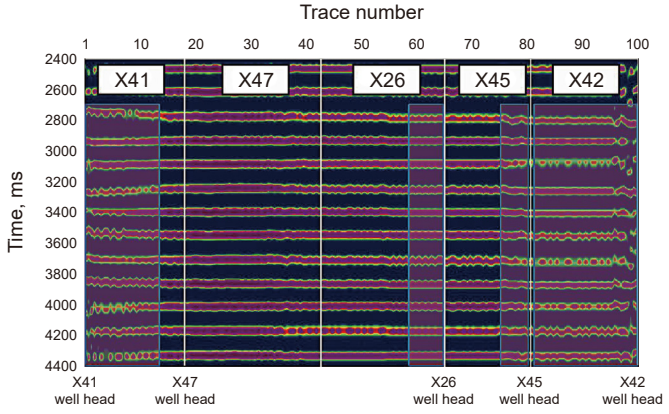

Fig. 14. First comparison of time-lapse imaging results of background noise data (July 20–July 31, the white vertical line is the dividing line between the data of the five wells).

increased significantly. This reveals that after this stop the water-flooding front still moves under the action of pressure. During the entire pressure flooding process of Well X45 (Fig. 19(c)), the oil production and gas production did not change regularly, and the

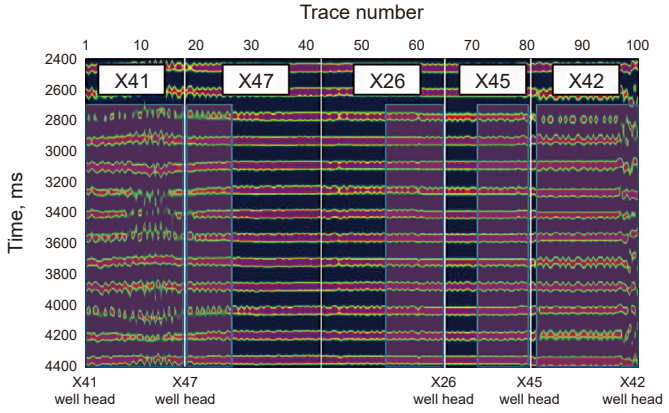

Fig. 15. Second comparison of time-lapse imaging results of background noise data (July 20–August 11).

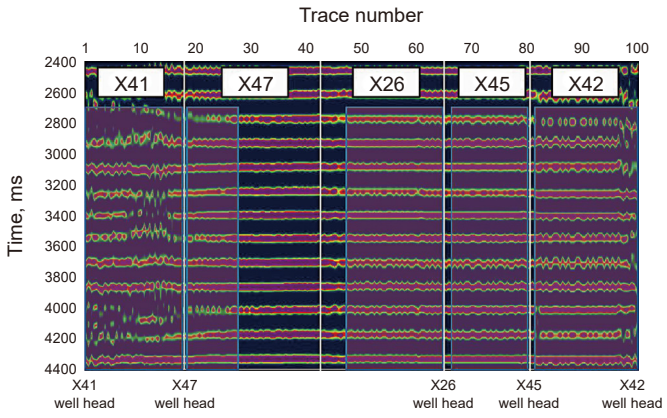

Fig. 16. Third comparison of time-lapse imaging results of background noise data (July 20–August 20).

production data fluctuated with the development of the operation, indicating that pressure flooding has an obvious driving effect on underground reservoirs. Well X42 (Fig. 19(d)) produced 100% water content by pressure flooding on July 28, and oil/gas production dropped significantly. Since July 28, both oil and gas production decreased obviously. On August 13, oil and gas production was close to zero. It can be seen from the data that the well was under pressure on July 28 and the water flood front reached the bottom of the well, but there were still other places connected that did not bring some oil and gas to the bottom of the well. After August 13, the flood front corresponding to this area also reached the bottom of the well and no oil or gas was produced. Well X41 (Fig. 19(e)) produced 100% water content by pressure flooding on August 4, and oil/gas production dropped sharply. This means that the well was penetrated and the water flood front reached the bottom.

5. Conclusions

Based on passive source seismic interference imaging and time-lapse seismic analysis, we propose a continuous and low-cost dynamic reservoir monitoring method to control the waterflooding front in oilfields. To do this, we carry out a series of specific operations and data screening on long-term passive source noise data collected at different time periods, and finally obtain the dynamic changes of underground reservoirs through time-lapse imaging analysis, thus allowing the entire process to be monitored in continuous. The results obtained first through a laboratory experiment with synthetic data and subsequently through a practical example with real field data demonstrate that the proposed method can be used to monitor the waterflooding front. The field data strongly support the results obtained through dynamic monitoring based on passive source seismic imaging and prove the effectiveness and feasibility of the proposed method.

It is worth noting that the goal of this method is not to perform structural imaging like conventional seismic methods, but to reflect changes in underground reservoirs through time-lapse imaging and similarity matrix analysis. In addition, as current seismic acquisition instruments are gradually beginning to have the ability to transmit in real time, when we image enough times, we can achieve a fast response monitoring. This paper is one of the few successful cases of applying the passive source time-lapse seismic method to oil field development. The proposed method has been used for many waterflooding monitoring experiments in some working areas of Shengli Oilfield. The monitoring cost is low and the results are reliable. This provides valuable guidance for future

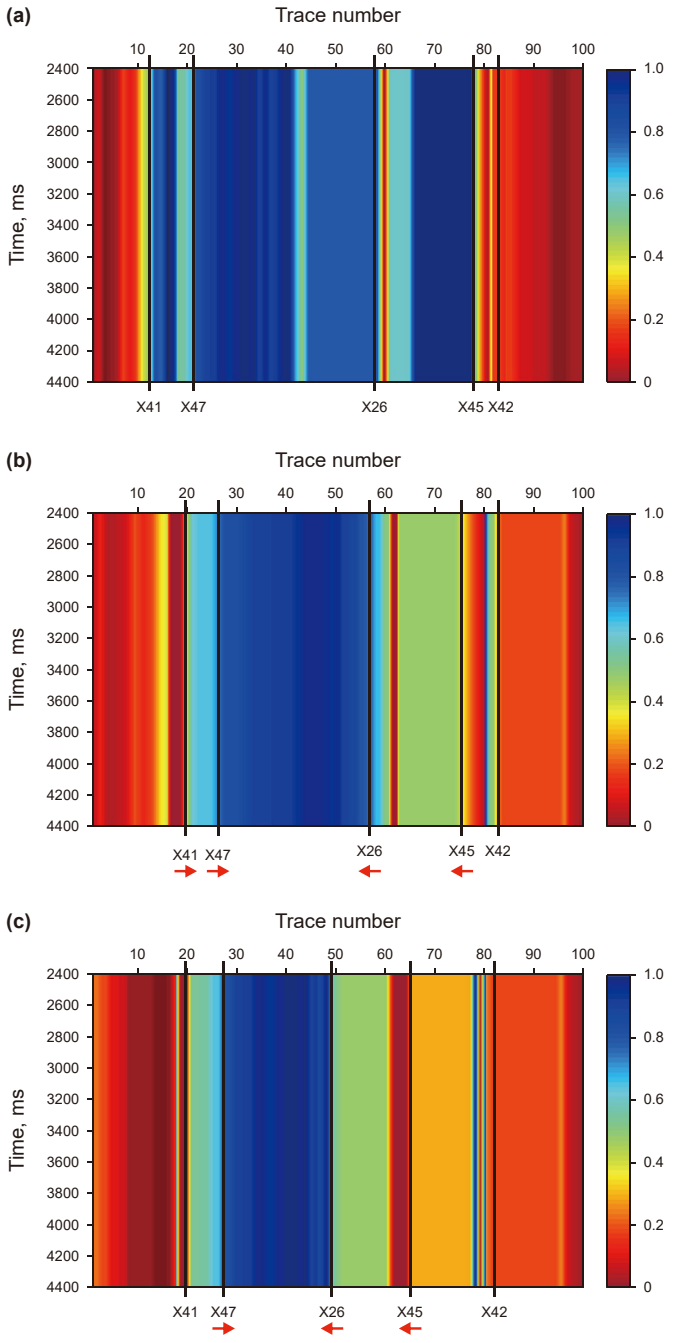

Fig. 17. Similarity matrix imaging results: **(a)** July 20–July 31; **(b)** July 20–August 11; **(c)** July 20–August 20 (The black vertical straight lines are the dividing lines of the abnormal area, which can be understood as the cutting edge of the waterflooding front. The red arrows indicate changes in the waterflooding front referred to the positions set by the black lines.).

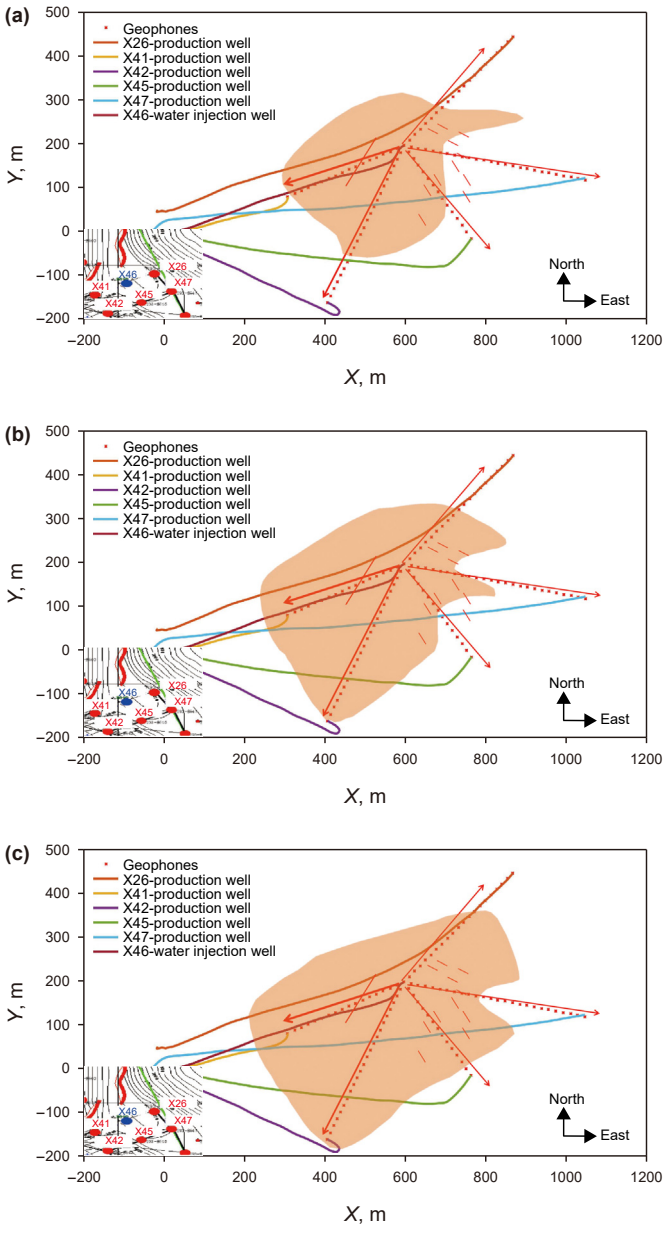

Fig. 18. Waterflooding front prediction results: **(a)** July 20–July 31; **(b)** July 20–August 11; **(c)** July 20–August 20. By projecting the position of the black line that marks the anomaly boundary (Fig. 17) onto the position of the corresponding geophone in the observation system, the waterflooding fronts can be obtained as time lapse (see colored irregular area). The lower left sub-image is a structural interpretation map of the work area, where the red line is a large fault in the work area.

developments and has enormous application potential. At present, we are trying to use this method for the long-term monitoring of a large-scale CO_2 flooding project in Xinjiang, China, which is likely to become a useful tool for CO_2 geological storage safety monitoring and help to control carbon dioxide emissions and the carbon footprint.

CRediT authorship contribution statement

Ying-He Wu: Writing – original draft, Software, Methodology. **Shu-Lin Pan:** Supervision, Formal analysis, Conceptualization. **Hai-Qiang Lan:** Funding acquisition, Writing-review & editing. **Jing-Yi Chen:** Visualization, Validation. **José Badal:** Writing – review & editing. **Yao-Jie Chen:** Investigation, Data curation. **Zi-Lin Zhang:** Resources, Project administration. **Zi-Yu Qin:** Visualization.

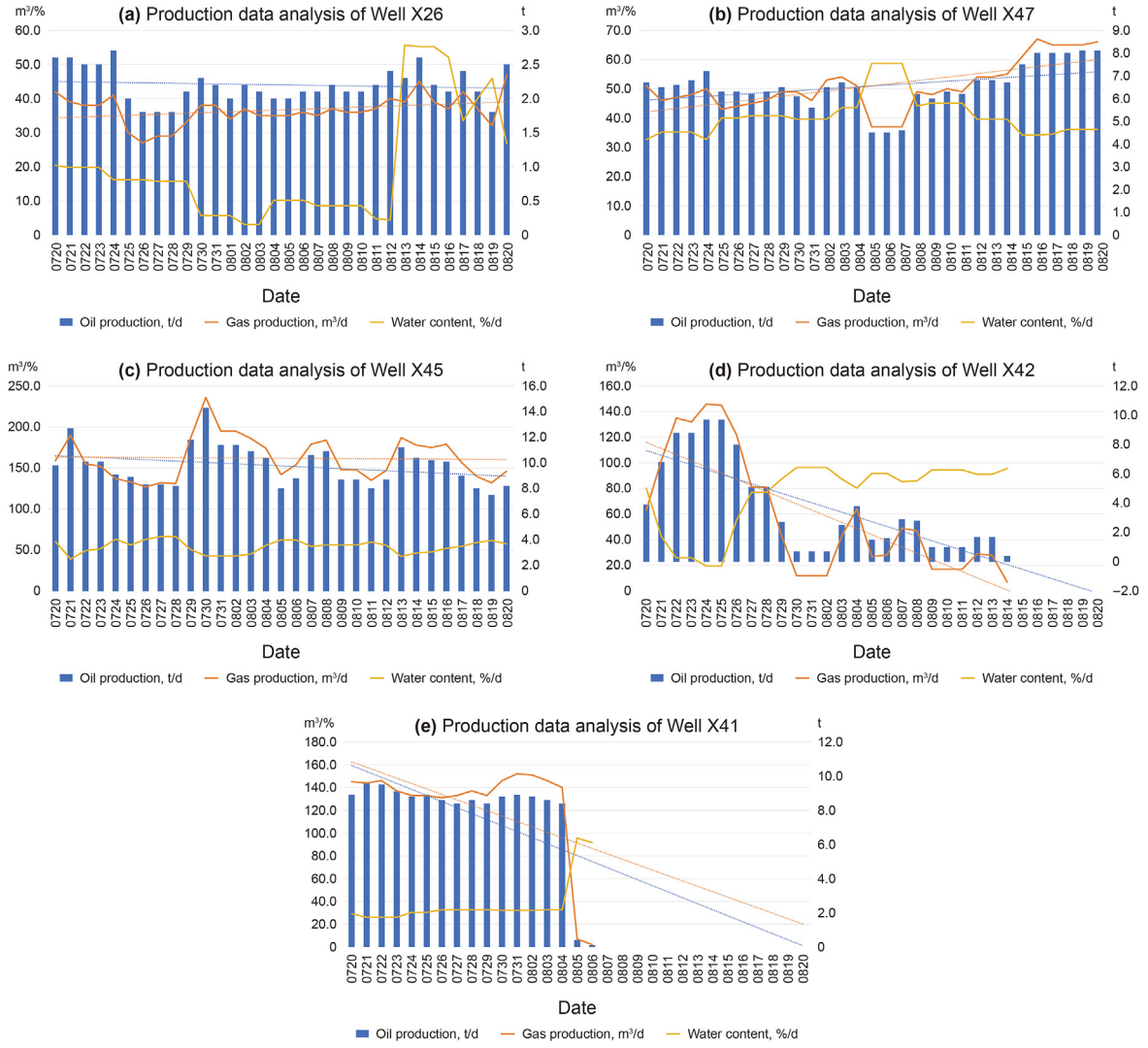

Fig. 19. In-situ production data of the five oil wells monitored in the target area (from top to bottom): **(a)** well X26; **(b)** well X47; **(c)** well X45; **(d)** well X42; **(e)** well X41. (The units of the coordinate axes are tons (t), cubic meters (m^3), and percentage (%)).

Conflict of interest

The authors declared that the research was conducted in the absence of any commercial or financial relationships that could be construed as a potential conflict of interest.

Acknowledgments

This work was supported by the CNPC-SWPU Innovation Alliance Technology Cooperation Project (2020CX020000), the National Natural Science Foundation of China (42022028), the Natural Science Foundation of Sichuan Province (24NSFSC0808), and the China Scholarship Council (202306440144).

References

Aki, K., 1957. Space and time spectra of stationary stochastic wave, with special reference to microtremors. Bull. Earthq. Res. Inst. 35, 415–456.

Almagro Vidal, C., Draganov, D., van der Neut, J., Drijkoningen, G., Wapenaar, K., 2014. Retrieval of reflections from ambient noise using illumination diagnosis. Geophys. J. Int. 198, 1572–1584. https://doi/10.1093/gji/ggu164.

Bensen, G.D., Ritzwoller, M.H., Barmin, M.P., Levshin, A.L., Lin, F., Moschetti, M.P., Shapiro, N.M., Yang, Y., 2007. Processing seismic ambient noise data to obtain reliable broad-band surface wave dispersion measurements. Geophys. J. Int. 169, 1239–1260. https://doi/10.1111/j.1365-246X.2007.03374.x.

Boullenger, B., Verdel, A., Paap, B., Thorbecke, J., Draganov, D., 2015. Studying CO_2 storage with ambient-noise seismic interferometry: a combined numerical feasibility study and field-data example for Ketzin, Germany. Geophysics 80 (1), Q1–Q13. https://doi/10.1111/j.1365-246X.2007.03374.x.

Chamarczuk, M., Malinowski, M., Nishitsuji, Y., 2019. Automatic 3D illumination-diagnosis method for large- N arrays: robust data scanner and machine-learning feature provider. Geophysics 84 (3), Q13–Q25. https://doi/10.1190/geo2018-0504.1.

Chamarczuk, M., Malinowski, M., Draganov, D., 2021. 2D body-wave seismic interferometry as a tool for reconnaissance studies and optimization of passive reflection seismic surveys in hardrock environments. J. Appl. Geophys. 187, 104288. https://doi.org/10.1016/j.jappgeo.2021.104288.

Chamarczuk, M., Malinowski, M., Draganov, D., Koivisto, E., Heinonen, S., Sanna Rötsä, S., 2022. Reflection imaging of complex geology in a crystalline environment using virtual-source seismology: case study from the Kylylahti polymetallic mine, Finland. Solid Earth 13, 705–723. https://doi/10.5194/se-2021-142.

Cheraghi, S., Craven, J.A., Bellefleur, G., 2015. Feasibility of virtual source reflection seismology using interferometry for mineral exploration: a test study in the Lalor Lake VMS mining area, Manitoba, Canada. Geophys. Prospect. 63, 833–848. https://doi/10.1111/1365-2478.12244.

Cheraghi, S., White, J., Draganov, D., Bellefleur, G., Craven, J.A., Roberts, B., 2017. Passive seismic reflection interferometry: a case study from the Aquistore CO_2 storage site, Saskatchewan, Canada. Geophysics 82 (3), B79–B93. https://doi/10.1190/geo2016-0370.1.

Claerbout, J.F., 1968. Synthesis of a layered medium from its acoustic transmission response. Geophysics 33 (2), 264. https://doi/10.1190/1.1439927.

Cotton, J., Chauris, H., Forgues, E., Hardouin, P., 2018. Time-lapse velocity analysis -

application to onshore continuous reservoir monitoring. Geophysics 83 (3), B105–B117. https://doi/10.1190/geo2017-0014.1.
De Freitas, J.M., 2011. Recent developments in seismic seabed oil reservoir monitoring applications using fibre-optic sensing networks. Meas. Sci. Technol. 22, 052001. https://doi/10.1088/0957-0233/22/5/052001.
Draganov, D., Wapenaar, K., Thorbecke, J., 2004. Passive seismic imaging in the presence of white noise sources. Lead. Edge 23, 889–892. https://doi/10.1190/1.1803498.
Draganov, D., Campman, X., Thorbecke, J., Verdel, A., Wapenaar, K., 2009. Reflection imaging from ambient seismic noise. Geophysics 74 (5), A63–A67. https://doi/10.1190/1.3193529.
Dullien, F.A.L., Dong, M., 2002. The importance of capillary forces in waterflooding: an examination of the Buckley-Leverett frontal displacement theory. J. Porous Media 5, 1–15. https://doi/10.1615/JPorMedia.v5.i1.10.
Fanchi, J.R., Pagano, T.A., 1999. State of the art of 4D seismic monitoring: the technique, the record, and the future. Oil Gas J. 97 (22), 38–43.
Fang, J., Liu, Y., Liu, G.F., 2022. Enhancing body waves in passive seismic reflection exploration: a case study in Inner Mongolia, China. Interpretation 10, B13–B24. https://doi/10.1190/int-2021-0113.1.
Gu, N., Chamarczuk, M., Gao, J., Malinowski, M., Zhang, H.J., 2021. Passive seismic structure imaging of a coal mine by ambient noise seismic interferometry on a dense array. Acta Geol. Sin. 95, 37–39. https://doi.org/10.1111/1755-6724.14826.
Guo, N.M., Wu, G.C., Shang, X.M., 2012. Application of mutual averaging method in non-repetitive time-lapse seismic data processing. Geophys. Prospect. Pet. 50 (6), 600–606 (in Chinese). https://doi/10.1007/s11629-011-1023-0.
Hoover, A.R., Burkhart, T., Flemings, P.B., 1999. Reservoir and production analysis of the K40 sand, South Timbalier 295, offshore Louisiana, with comparison to time-lapse (4-D) seismic results. AAPG (Am. Assoc. Pet. Geol.) Bull. 83, 1624–1641. https://doi/10.1190/1.1886167.
Hartstra, I.E., Almagro Vidal, C., Wapenaar, K., 2017. Full-field multidimensional deconvolution to retrieve body-wave reflections from sparse passive sources. Geophys. J. Int. 210 (2), 609–620. https://doi/10.1093/gji/ggx120.
Ivandic, M., Bergmann, P., Kummerow, J., Huang, F., Juhlin, C., Lueth, S., 2018. Monitoring CO_2 saturation using time-lapse amplitude versus offset analysis of 3D seismic data from the Ketzin CO_2 storage pilot site, Germany. Geophys. Prospect. 66, 1568–1585. https://doi/10.1111/1365-2478.12666.
Ivanova, A., Kashubin, A., Juhojuntti, N., Kummerow, J., Henninges, J., Juhlin, C., Lüth, S., Ivandic, M., 2012. Monitoring and volumetric estimation of injected CO_2 using 4D seismic, petrophysical data, core measurements and well logging: a case study at Ketzin, Germany. Geophys. Prospect. 60, 957–973. https://doi/10.1111/j.1365-2478.2012.01045.x.
Jones, G.A., Raymer, D., Chambers, K., Kendall, J.M., 2010. Improved microseismic event location by inclusion of a priori dip particle motion: a case study from Ekofisk. Geophysical prospecting 58 (5), 727–737. https://doi.org/10.1111/j.1365-2478.2010.00873.x.
Jupe, A., Cowles, J., 1998. Microseismic monitoring: listen and see the reservoir. World Oil 219, 171–174.
Jackson, M.D., Muggeridge, A.H., 2000. Effect of discontinuous shales on reservoir performance during horizontal waterflooding. SPE J. 5, 446–455. https://doi/10.2118/69751-PA.
Lan, H.Q., Zhang, Z.J., 2011. Comparative study of the free-surface boundary condition in two-dimensional finite-difference elastic wave field simulation. J. Geophys. Eng. 8, 275–286. https://doi/10.1088/1742-2132/8/2/012.
Lei, Y.S., Ning, H.X., Xiao, H., Zhang, D.Z., Wang, J.F., Ren, Y.Y., 2018. Joint application of node and wired instrument in high altitude mountain area. SEG International Exposition and Annual Meeting. https://doi/10.1190/SEGAM2018-2991537.1.
Lekan, L., Blunt, M.J., King, P.R., 2020. A salinity cut-off method to control numerical dispersion in low-salinity waterflooding simulation. J. Pet. Sci. Eng. 184, 106586. https://doi/10.1016/j.petrol.2019.106586.
Li, Y.Q., 2006. Experimental Study on Physical Simulation of Polymer Flooding Large Plane Model. Graduate University of Chinese Academy of Sciences, Beijing, China.
Li, X.L., Ling, D.D., Li, D.C., 2015. Application of interferometric imaging in Shuangan goaf detection. Prog. Geophys. 30, 2188–2192 (in Chinese). https://doi/10.6038/PG20150526.
Liu, G.F., Liu, Y., Meng, X.H., Liu, L.B., Su, W.J., Wang, Y.Z., Zhang, Z.F., 2021. Surface wave and body wave imaging of passive seismic exploration in shallow coverage area application of Inner Mongolia. J. Geophys. 64, 937–948. https://doi/10.6038/cjg2021O0064.
Maxwell, S.C., Rutledge, J., Jones, R., Fehler, M., 2010. Petroleum reservoir characterization using downhole microseismic monitoring. Geophysics 75 (5), 1SO–Z116. https://doi/10.1190/1.3477966.
Meng, L.B., Zheng, J., Yang, R.Z., Peng, S.P., Sun, Y., Xie, J.Y., Li, D.W., 2023. Microseismic monitoring technology developments and prospects in CCUS injection engineering. Energies 16, 3101. https://doi/10.3390/en16073101.
Rickett, J., Claerbout, J.F., 1999. Acoustic daylight imaging via spectral factorization: helioseismology and reservoir monitoring. Lead. Edge 18, 957–960. https://doi/10.1190/1.1820854.
Schuster, G.T., Rickett, J., 2001. Daylight imaging in V(x,y,z) media. Stanford Exploration Project and SEP Report 105, 209–227.
Schuster, G.T., 2009. Seismic Interferometry. Cambridge university press.
Shi, Y.M., Yao, F.C., Xie, G.S., Liu, W.L., 2006. A study of the method for time-lapse seismic monitoring of waterflooding front and its application. Chin. J. Geophys. 49, 1198–1205. https://doi/10.1002/cjg2.925cjg2931.
Sabra, K.G., 2009. Effect of noise sources motion on the performance of passive imaging from ambient noise cross-correlation. J. Acoust. Soc. Am. 125, 2512. https://doi/10.1121/1.4783433.
Tsuji, T., Ikeda, T., Johansen, T.A., Ruud, B.O., 2015. Time-lapse seismic profiles derived from passive seismic interferometry in fluid-injection experiments. In: SEG International Exposition and Annual Meeting. https://doi/10.1190/segam2015-5854972.1.
Wang, Z.J., Hirsche, W.K., 1991. George Sedgwick.Seismic monitoring of water floods?—a petrophysical study. Geophysics 56 (10), 1614. https://doi/10.1190/1.1442972.
van der Neut, J., Thorbecke, J., Mehta, K., Slob, E., Wapenaar, K., 2011. Controlled-source interferometric redatuming by crosscorrelation and multidimensional deconvolution in elastic media. Geophysics 76 (4), SA63–SA76. https://doi/10.1190/1.3580633.
Wang, Z., Cates, M.E., Langan, R.T., 1998. Seismic monitoring of a CO_2 flood in a carbonate reservoir: a rock physics study. Geophysics 63 (5), 1604–1617. https://doi/10.1190/1.1444457.
Wang, L.D., Chen, W.B., Cheng, J., 2016. Analyses and applications of the second-order cross correlation in the passive imaging. Commun. Comput. Phys. 19, 1191–1220. https://doi/10.4208/cicp.scpde14.26s.
Wang, B., Nie, Q.H., Chen, J.E., Wang, C.Y., 2021. Application of 4D multi-component seismic survey in dynamic reservior monitoring. Oil Geophys. Prospect. 56, 340–345 (in Chinese). https://doi/10.13810/j.cnki.issn.1000-7210.2021.02.016.
Wang, C.S., Sun, Z.X., Sun, Q.J., Zhang, L., Zhang, X.Q., 2021. Comprehensive evaluation of waterflooding front in low-permeability reservoir. Energy Sci. Eng. 9 (9), 1394–1408. https://doi/10.1002/ese3.948.
White, D., 2013. Seismic characterization and time-lapse imaging during seven years of CO_2 flood in the Weyburn field, Saskatchewan, Canada. Int. J. Greenh. Gas Control 16S, 78–94. https://doi/10.1016/j.ijggc.2013.02.006.
Wulff, A.M., Mjaaland, S., 2002. Seismic monitoring of fluid fronts: an experimental study. Geophysics 67 (1), 221–229. https://doi/10.1190/1.1451622.
Wapenaar, K., Draganov, D., Snieder, R., Campman, X., Verdel, A., 2010. Seismic Interferometry: Tutorial on Seismic Interferometry: Part 1—Basic Principles and Applications.
Xu, Y.H., Wang, T.G., Chen, N.X., Yang, C.M., Wang, Q.L., 2012. DBT parameters and dynamic monitoring during reservoir development, and distribution region prediction of remaining oil. A case study on the Sha-3 oil reservoir in the Liubei region, Nanpu sag. Sci. China Earth Sci. 55, 2018–2025. https://doi/10.1007/s11430-012-4537-6.
Xu, Z., Juhlin, C., Gudmundsson, O., Zhang, F.J., Yang, C., Kashubin, A., Luth, S., 2012. Reconstruction of subsurface structure from ambient seismic noise: an example from Ketzin, Germany. Geophys. J. Int. 189, 1085–1102. https://doi/10.1111/J.1365-246X.2012.05411.X.
Yan, J.H., Xu, Y.N., Zhu, H.L., Du, Y.B., Chu, Z.H., 2005. Research and Field Application of Waterflooding and Fracture Monitoring Technology. Fault-Block Oil & Gas Field, pp. 59–61.
Zeng, D., Peng, X., Fu, D., Hu, J., Wu, X., Zhang, J., 2018. Development dynamic monitoring technologies used in the Puguang high-sulfur gas field. Nat. Gas. Ind. 38, 63–69. https://doi/10.1016/j.ngib.2018.10.001.
Zhang, F.J., Xu, Z., Juhlin, C., Ivandic, M., Han, L.G., Zhang, P., 2022. Passive seismic interferometry imaging. An example from the Ketzin pilot CO2 geological storage site. J. Appl. Geophys. 205, 104765. https://doi/10.1016/j.jappgeo.2022.104765.
Zhao, C.F., Jiang, H.Q., Chen, M.F., Li, X.S., 2006. Waterflooding state law of fractured sandstone reservoirs. Journal of Xi 'an Shiyou University (Natural Science Edition) 21, 26–28.
Zhao, X.Z., Deng, Z.W., Bai, X.M., Yuan, S.H., Li, H.D., Tang, C.Z., 2015. Environmental seismic filed operations in grass-lands, Erlian Basin. Oil Geophys. Prospect. 50, 14–19 (in Chinese). https://doi/10.13810/j.cnki.issn.1000-7210.2015.01.003.